Atmospheric
Chemistry
and Physics
Discussions

1 **Vehicle-based in-situ observations of the water vapor isotopic**

2 **composition across China: spatial and seasonal distributions and**

3 **controls**

4 Di Wang[1,2,3], Lide Tian[1,3], Camille Risi[2], Xuejie Wang[1,3], Jiangpeng Cui[4], Gabriel J.

5 Bowen[5], Kei Yoshimura[6], Zhongwang Wei[7], Laurent Z.X Li[2]

6 *[1] Institute of International Rivers and Eco-security, Yunnan University, Kunming 650500,*

7 *Yunnan, China*

8 *[2] Laboratoire de Météorologie Dynamique, IPSL, CNRS, Sorbonne Université, Paris 75006,*

9 *France*

10 *[3] Yunnan Key Laboratory of International Rivers and Transboundary Eco–security,*

11 *Kunming 650500, Yunnan, China*

12 *[4] Sino-French Institute for Earth System Science, College of Urban and Environmental*

13 *Sciences, Peking University, Beijing 100871, China*

14 *[5] Department of Geology and Geophysics, and Global Change and Sustainability Center,*

15 *University of Utah, Salt Lake City, Utah 84108, USA*

16 *[6] Institute of Industrial Science, The University of Tokyo, Tokyo113-8654, Japan*

17 *[7] School of Atmospheric Sciences, Sun Yat-sen University, Guangzhou 510275, Guangdong,*

18 *China*

19 *Corresponding author: wangdishi.mp@hotmail.com; ldtian@ynu.edu.cn.*

20

Atmospheric
Chemistry
and Physics
Discussions

21   **Abstract**

22   Stable water isotopes are natural tracers in the hydrological cycle and have been applied
23   in hydrology, atmospheric science, ecology, and paleoclimatology. However, the factors
24   controlling the isotopic distribution, both at spatial and temporal scales, are debated in East
25   Asia. For the first time, we made large scale (order 10000 km) continuous observations of near-
26   surface vapor isotopes across China in both pre-monsoon and monsoon seasons, using a newly-
27   designed vehicle-based vapor isotope monitoring system. For both seasons, the observed
28   variations along the sampling route are mainly due to spatial variations, and marginally
29   influenced by synoptic-scale variations. The data thus documents the spatial and seasonal
30   variability of vapor isotopes. The spatial variations of vapor $\delta^{18}O$ are mainly controlled by
31   Rayleigh distillation during the pre-monsoon period, but significantly influenced by different
32   moisture sources, continental recycling processes and convection during moisture transport
33   during the monsoon period. The seasonal variation of vapor $\delta^{18}O$ reflects the influence of the
34   summer monsoon convective precipitation in southern China, and a dependence on temperature
35   in the North. The spatial and seasonal variations in d-excess reflect the different moisture
36   sources and the influence of continental recycling. The isotope-incorporated global spectral
37   model (Iso-GSM) successfully captures the spatial variation of vapor $\delta^{18}O$ during the pre-
38   monsoon period owing to the large latitudinal contrast in humidity and temperature, the overall
39   performance is weaker during the monsoon period. These results provides an overview of the
40   spatial distribution and seasonal variability of water isotopic composition in East Asia and their
41   controlling factors, and emphasize the need to interpret proxy records in the context of the
42   regional system and moisture sources.

43   **Keywords:** Vapor isotopes, Spatial distribution, Seasonal difference, East Asia, Moisture
44   sources, Moisture propagation

45   **1. Introduction**

46   Isotopic equilibrium and kinetic fractionation produce a natural labeling effect within the
47   global water cycle. Stable water isotopes have thus been applied to study a wide range of
48   hydrological and climatic processes (Gat, 1996;Bowen et al., 2019;West et al., 2009). Stable
49   isotopic signals recorded in natural precipitation archives are used in the reconstructions of
50   ancient continental climate and hydrological cycles due to their strong spatial relationship with
51   local meteorological conditions. Examples include ice cores (Thompson, 2000;Yao et al.,
52   1991;Tian et al., 2006), tree-ring cellulose (Liu et al., 2017), stalagmites (Van Breukelen et al.,
53   2008), and lake deposits (Hou et al., 2007). However, unlike in polar ice cores, isotopic records
54   in Tibetan ice cores (Thompson et al., 1997) have encountered challenges as temperature
55   proxies (Brown et al., 2006). Recent advances in understanding controls on precipitation and
56   ice core isotopes in Asian monsoon regions highlight the significant role of large regional
57   atmospheric circulation, e.g. El Niño/Southern Oscillation and Interdecadal Pacific Oscillation
58   Index (Cai and Tian, 2016;Yang et al., 2016;Vuille and Werner, 2005). The controlling factors
59   of water isotopes in low-latitude regions also differ with the time scales (e.g., Shi et al.(2020)).
60   Additional data and analysis refining our understanding of controls on the spatial and temporal

61   variation of water isotopes in low-latitude regions such as East Asia therefore are needed.

62   Unlike precipitation, water vapor enters all stages of the hydrological cycle, experiencing
63   frequent and intensive exchange with other water phases, in particular, directly linked with
64   water isotope fractionation. Furthermore, vapor isotopes can be measured in regions and
65   periods without precipitation, and therefore, have significant potential to trace how water is
66   transported, mixed, and exchanged (Galewsky et al., 2016;Noone, 2008), and to diagnose large-
67   scale water cycle dynamics. Water vapor isotope data have been applied to systems ranging
68   from the marine boundary layer to continental recycling, from tropical convection to polar
69   climate reconstructions (Galewsky et al., 2016).

70   The development of laser-based spectroscopic isotope analysis made the precise, high-
71   resolution and real-time measurements of both vapor $\delta^{18}O$ and $\delta^{2}H$ available in recent decades.
72   However, most of the in-situ observation are station-based (e.g., Li et al.(2020), Tian et
73   al.(2020), Steen-Larsen et al.(2017)), or performed during ocean cruises (Thurnherr et al.,
74   2020;Bonne et al., 2019;JingfengLiu et al., 2014;Kurita, 2011;Benetti et al., 2017). These
75   observations provided new insight on moisture sources, synoptic influences, and sea surface
76   evaporation fractionation processes. Few observations are available over the continent, where
77   moisture sources are more complex (Bailey et al., 2013). To go one step further, continuous
78   monitoring of near-surface vapor isotopes at broad continental scales would support research
79   on how large-scale circulation and synoptic processes affect spatial and seasonal variations in
80   isotopic composition.

81   This paper presents a unique and novel isotope dataset consisting of vehicle-based
82   spatially continuous near-surface vapor isotopes across a large spatial scale in China during the
83   pre-monsoon and monsoon periods. The data provide a detailed description of the spatial and
84   seasonal variability of vapor isotopes and their controlling mechanisms in the middle and low
85   latitudes. Our results reveal two types of isotopic patterns: (1) spatial variations at the regional
86   scale for a given season, and (2) synoptic-scale variations that locally disturb the seasonal-mean
87   variations. To disentangle these two effects and their causes, we exploit simulations from the
88   isotope-incorporated global spectral model (Iso-GSM). Collectively, these data and analyses
89   provide refined understanding of how the interaction of the summer monsoon and westerly
90   circulation control water isotope ratios in East Asia.

91   **2.   Data and methods**

92   2.1 Geophysical description

93   China has a typical monsoon climate (Wang, 2002;Domrös and Peng, 2012). Large parts
94   of the country are affected by the Indian monsoon and the East Asian monsoon in summer
95   (Fig.1), which bring humid marine moisture from the Indian Ocean, South China Sea, and
96   Northwestern Pacific Ocean. During the non-monsoon seasons, the Westerlies influence most
97   of northern China (Fig.1). Dry intrusion brings extremely cold and dry air masses. Occasional
98   moisture flow from the Indian Ocean and/or Pacific Ocean brings moisture to southern China.
99   This seasonal patterns of water vapor transport are also imprinted in the observed precipitation
100   isotopes (Araguás-Araguás et al., 1998;Tian et al., 2007;Wright, 1993;Mei'e et al., 1985;Tan,
101   2014).

102   We conducted two campaigns to monitor vapor isotopes across a large part of China during
103 the pre-monsoon (3rd to 26th March, 2019) and the monsoon (28th July to 18th August, 2018)
104 periods, using a newly designed vehicle-based vapor isotope monitoring system (Fig.S1). The
105 two campaigns run along almost the same route, with slight deviation in the far northeast of
106 China (Fig.1). Our vehicle started from Kunming city in southwestern China, traveled northeast
107 to Harbin, then turned to northwestern China (Hami), and returned to Kunming. The expedition
108 traversed most of eastern China, with a total distance of above 10000km for each campaign.
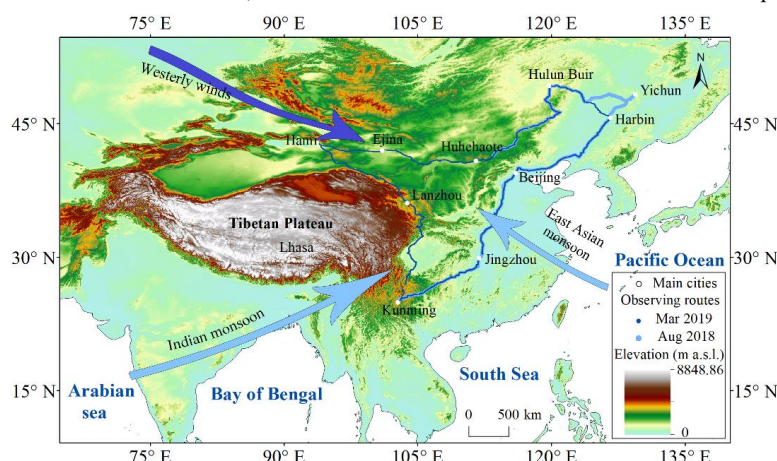

110 Fig.1. Topographical map of China, showing survey routes and the main atmospheric
111 circulation systems (arrows). Dark blue dots indicate the observation route for the 2019 pre-
112 monsoon period, and light blue dots show the observation route for the 2018 monsoon period,
113 with a slight deviation in the northeast.
114

115 2.2 Vapor isotope measurements

116   2.2.1 Isotopic definitions.
117   Isotopic compositions of samples were reported as the relative deviations from the
118 standard water (Vienna Standard Mean Ocean Water, VSMOW), using the δ-notion (McKinney
119 et al., 1950), where R_{sample} and R_{VSMOW} are the isotopic ratios ($H_2^{18}O/H_2^{16}O$ for $\delta^{18}O$, and
120 $^1H^2H^{16}O/H_2^{16}O$ for δ^2H) of the sample and of the VSMOW, respectively:
121     $\delta = (R_{sample}/R_{VSMOW}-1)*1000$ (1)
122   The second-order deuterium excess parameter are computed based on the commonly used
123 definition (Dansgaard, 1964)：
124   d-excess $=\delta^2H-8*\delta^{18}O$ (2)
125   2.2.2 Instrument
126   We used a Picarro 2130i CRDS water vapor isotope analyzer fixed on a vehicle to obtain
127 continuous measurements of near-surface vapor isotopes along the route. The analyzer was
128 powered by a lithium battery on the vehicle, enabling over 8 hours operation with a full charge.
129 Therefore, we only made measurements in daytime and recharged the battery at night. The
130 ambient air inlet of the instrument was connected to the outside of the vehicle, which was 1.5
131 m above ground, with a waterproof cover to keep large liquid droplets from entering. A portable

132 GPS unit was used to record position data along the route. The measured water vapor mixing
133 ratio and the $\delta^{18}O$ and δ^2H were obtained with a temporal resolution of ~1 second. The dataset
134 present in this study had been averaged to a 10-min temporal resolution after calibration, with
135 the horizontal footprint of about 15 km.

136 A standard delivery module (SDM) was used for the vapor isotope calibration during the
137 surveys. The calibration protocols consists of humidity calibration (section 2.2.3), standard
138 water calibration (section 2.2.4), and error estimation (section 2.2.5), following the methods of
139 Steen-Larsen et al.(2013).

140 2.2.3 Humidity calibration

141 The measured vapor isotopes are sensitive to air humidity (JingfengLiu et al.,
142 2014;Galewsky et al., 2016), which vary substantially across our sampling route. Hence, we
143 develop a humidity calibration by measuring a water standard at different water concentration
144 settings using the SDM. We define a reference level of 20,000 ppm of vapor humidity for our
145 analysis (Eq. 3), the calibrated vapor isotope with different air humidity would be:

146 $$\delta\text{-}_{humidity\ calibration} = \delta\text{-}_{measured} - f\ (humidity_{measured} - 20000) \qquad (3)$$

147 where $\delta\text{-}_{measured}$ represents the measured vapor isotopes (the raw data), $\delta\text{-}_{humidity\ calibration}$ denotes
148 the calibrated vapor isotopes, f is the calibrated humidity correction term, and humidity is in
149 ppm.

150 We performed the humidity calibration before and after each campaign. In the calibration,
151 the setting of humidity covered the actual range of humidity in the field. In the dry pre-monsoon
152 period of 2019, the humidity was less than 5000 ppm along a large part of the route. In this case,
153 we performed additional calibration tests with the humidity less than 5000 ppm after the field
154 observations to guarantee the accuracy of the calibration results. The humidity-dependence
155 calibration function is considered constant throughout each campaign (which each lasted less
156 than 24 days).

157 2.2.4 Measurement normalization

158 All measured vapor isotope values were calibrated to the VSMOW-SLAP scale using two
159 laboratory standard waters ($\delta^{18}O = -10.33‰$ and $\delta^2H = -76.95‰$, $\delta^{18}O = -29.86‰$ and $\delta^2H = $
160 $-222.84‰$) covering the range of the expected ambient vapor values. We made the
161 normalization test prior to the daily measurements (two humidity levels for each standard
162 water). We adjusted the amount of the liquid standard injected everyday to keep the humidity
163 of the standard waters consistent with the outside vapor measurements. Our calibration shows
164 that no significant drift of the standard values were observed over time in the observation
165 periods.

166 2.2.5 Error estimation

167 We estimate the uncertainty based on the error between the measured (after calibration)
168 and true values of the two standards used during the campaigns. The estimated uncertainty is
169 in the range of -0.05~0.17 for $\delta^{18}O$, 0.11~1.19 for δ^2H, and -0.81~1.23‰ for d-excess during
170 the pre-monsoon period of 2019, with the humidity ranges from 2000 ppm to 29000 ppm.
171 During the monsoon period of 2018, the range of uncertainty is -0.10~0.55‰ for $\delta^{18}O$, -
172 0.94~3.74‰ for δ^2H, and -1.18~1.49‰ for d-excess, with the humidity ranges from 4000 to
173 34000 ppm.

174 2.2.6 Data processing

175 A few isotope measurements with missing GPS information were excluded from the

176   analysis. Since we want to focus on large-scale variations, we also removed the observations
177   during raining or snowing, to avoid situations where hydrometeor evaporation significantly
178   influenced the observations (Tian et al., 2020). Such data represents only 0.03% and 0.05% of
179   our observations, respectively (totally 48 data during pre-monsoon season and 59 data during
180   the monsoon season). We observed several d-excess pulses with extremely low values as low
181   as −18.0‰ during the pre-monsoon period and -4.9‰ during the monsoon period. These low
182   values are unusual in previous natural vapor isotope studies and occurred mostly when the
183   measurement vehicle was entering or leaving cities and/or stuck in traffic jams. We assume
184   these abnormal data are significantly influenced by fuel combustion (Gorski et al., 2015), and
185   we also excluded these data (133 data points during the pre-monsoon period and 62 data points
186   during the monsoon period, represents 0.10% and 0.06% of our observations, respectively) in
187   the discussion on the general spatial feature (except Fig.2). Alternatively, we add a short
188   discussion about this influence specifically in section 4.8.

189   2.3 Meteorological observations and back-trajectory calculation

190   We fixed a portable weather station on the roof of the vehicle to measure air temperature
191   (T), dew-point temperature (T_d), air pressure (Pres) and relative humidity (RH). All sensors
192   were located near the ambient air intake. The specific humidity (q) of the near-surface air was
193   calculated from the measured T_d and Pres. Meteorological data, GPS location data and vapor
194   isotope data were synchronized according to their measurement times.
195   National Centers for Environmental Prediction/ National Center for Atmospheric Research
196   (NCEP/NCAR) 2.5-deg global reanalysis data are used to determine the large-scale factors
197   influencing the spatial pattern of the vapor isotopes, including the surface T, q, U-wind and V-
198   wind,   and   RH,   which   are   available   at
199   https://psl.noaa.gov/data/gridded/data.ncep.reanalysis.surface.html.   Some   missing
200   meteorological data (during the pre-monsoon period: q on 8th March and 18th March 2019;
201   during the monsoon period: T and q from 28th July to 31st July, q on 5th August) along the survey
202   routes due to instrument failure are acquired from the NCEP/NCAR reanalysis data. To match
203   the vapor isotope data along the route, we linearly interpolate the NCEP/NCAR data to the
204   location and time of each measurement. The interpolated T and q from NCEP/NCAR are highly
205   correlated with our measurement as shown in Figure 2h and j. The precipitation amount (P)
206   from   the   Global   Precipitation   Climatology   Project   (GPCP)   are   used
207   (https://www.ncei.noaa.gov/data/global-precipitation-climatology-project-gpcp-daily/access/).
208   The   outgoing   longwave   radiation   (OLR)   data   can   be   obtained   from   NOAA
209   (http://www.esrl.noaa.gov/psd/data/gridded/data.interp_OLR.html).
210   To trace the geographical origin of the air masses, we select the driving locations every 2
211   hours as starting points for the backward trajectories, and make 10-day back-trajectories from
212   1000 m above ground using the Hybrid Single Particle Lagrangian Integrated Trajectory Model
213   4 (HYSPLIT4) model (Draxler and Hess, 1998). The T, q, P and RH along the back-trajectories
214   are also interpolated by HYSPLIT4 model. The HYSPLIT-compatible meteorological dataset
215   of   the   Global   Data   Assimilation   System   (GDAS)   is   used   (available   at
216   ftp://arlftp.arlhq.noaa.gov/pub/archives/gdas1/).

217   2.4 General circulation model simulation

218   To first validate the simulation results of the isotope-enabled general circulation model
219   (GCM) on spatial and seasonal scale during our observation periods, and finally to disentangle
220   the spatial and synoptic influence, we use surface layer variables from the Iso-GSM simulations
221   (Yoshimura and Kanamitsu, 2009), which has a latitude resolution of 1.915° and a longitude
222   resolution of 1.875°. When interpolating daily/temporal-mean outputs, we select the nearest
223   Iso-GSM grid point for a given latitude, longitude and date/time periods of each measurement.
224   Because of the coarse resolution of the model, there is a difference between the altitude
225   observed along the sampling route and that of the nearest grid point. Therefore, we correct the
226   outputs of iso-GSM for this altitude difference (the method is given in III. Supplementary Text).

227   **3   Results**

228   3.1 Spatial variations

229   Our survey of the vapor isotopes yields two snapshots of the isotopic distribution along
230   the route. The observed temporal variations along the route for a given period represent a
231   mixture of synoptic-scale perturbations, and of seasonal-mean spatial distribution. In section
232   4.7, simulation results will show that the contribution of seasonal-mean spatial variations
233   dominate. Therefore, the temporal variations observed along the route for a given period mainly
234   reflect spatial variations.
235   Figure 2 shows the variations of observed 10-min averaged surface vapor $\delta^{18}O$ and d-
236   excess along the survey route across China during the pre-monsoon and monsoon campaigns.
237   The figure also shows the concurrent meteorological data from the weather station installed on
238   the vehicle and the water vapor content recorded by the Picarro water vapor isotope analyzer
239   as a comparison. We extract daily precipitation amount (P-daily) and temporal-mean
240   precipitation amount for the sampling dates (P-mean) (mm/day) from GPCP. The vapor $\delta^{18}O$
241   shows high magnitude variations in both seasons. A general decreasing-increasing trend
242   overlapped with short-term fluctuations is observed during the pre-monsoon period, whereas
243   no general trend but frequent fluctuations characterized the monsoon period. The $\delta^{18}O$ range is
244   much larger during the pre-monsoon period (varying between -44‰ and -8‰) than during the
245   monsoon period (from -11‰ to -23‰). Most measured vapor d-excess values ranges from 5 to
246   25‰ during the pre-monsoon period and from 10 to 22‰ during the monsoon period.
247   Comparison with the concurrently observed meteorological data shows a robust air
248   temperature (T) dependence of the vapor $\delta^{18}O$ variations. In particular, the general trend of $\delta^{18}O$
249   is roughly consistent with T variation during the pre-monsoon period (Fig.2a and g). During
250   the pre-monsoon period, humidity (Fig.2e and i), P-mean (Fig.2k) and vapor $\delta^{18}O$ (Fig.2a) are
251   much higher in southwestern China (at the beginning and end of the campaign) than in any
252   other regions. Humidity, q, and P-mean also vary consistently throughout the route during the
253   monsoon period (Fig.2f, j, l). Synoptic effects on the observed vapor isotopes are discussed in
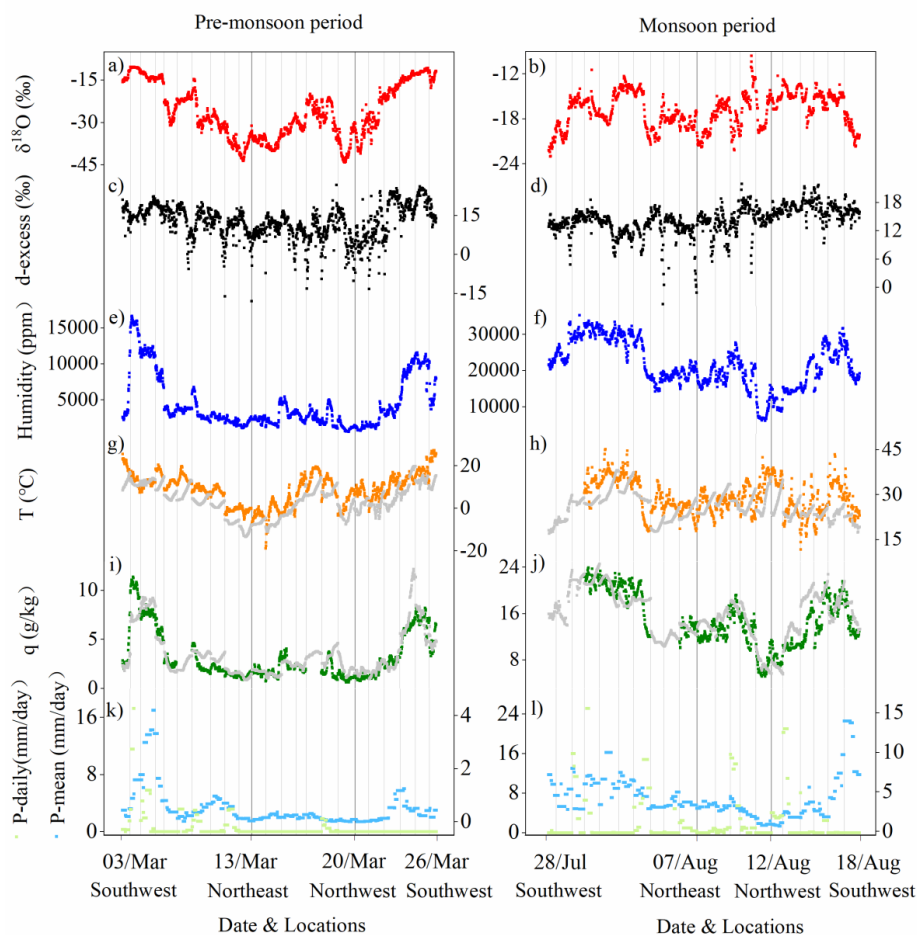254   detail in Section 4.3.

255 Fig.2. Measured vapor isotopic compositions and concurrent meteorological conditions along
256 the survey routes during the pre-monsoon period (the left panel) and monsoon period (the right
257 panel). (a, b) vapor $\delta^{18}O$ (‰); (c, d) vapor d-excess (‰); (e, f) vapor humidity (ppm); (g, h) air
258 temperature T (℃); (i, j) specific humidity q (g/kg), (k, l) the daily precipitation amount P-daily
259 (mm/day) and temporal-mean precipitation amount for the sampling dates P-mean (mm/day)
260 extract from GPCP. Notes: the gray dots are T and q linearly interpolate from NCAR reanalysis
261 to compensate for missing observations; Gray vertical lines space the observations for one day.
262

263 The spatial distribution of the observed vapor $\delta^{18}O$ and d-excess during the two surveys in
264 different seasons are presented in Figure 3. During the pre-monsoon period, we find a south-
265 north gradient of vapor $\delta^{18}O$ (Fig.3a). The vapor $\delta^{18}O$ ranges from -8~ -16‰ in southern China
266 to as low as -24 ~ -44‰ in the North. Temperature also shows a strong spatial dependence
267 during this period with relatively warm conditions in southern China and cold in the North
268 (Fig.S2 a). The apparent "temperature effect", wherein low local temperatures and low water
269 isotope values are correlated, has also been widely reported in studies of precipitation isotopes
270 in the non-monsoon season in China (Zhao et al., 2012;Liu et al., 2014;Johnson and Ingram,

272   2004). A roughly similar spatial pattern is observed for the vapor d-excess during the pre-
273   monsoon period (Fig.3c). The d-excess value ranges from 10 to 30‰ in southern China and
274   from -10 to +20‰ (most observations with values from 5 to +20‰) in northern China. In
275   previous studies, a higher precipitation d-excess during the pre-monsoon period was also
276   observed in the Asian monsoon region owing to the lower relative humidity (RH) at the surface
277   in the moisture source region (Tian et al., 2007;Jouzel et al., 1997). The same reason probably
278   explains the higher vapor d-excess in southern China observed here. The lower d-excess values
279   (as low as −10‰ to 10‰) in northern China (between 38°N and 51°N) have rarely been
280   reported in earlier studies. The spatial distribution of the observed vapor d-excess could reflect
281   the general latitudinal gradient of d-excess observed at the global-scale, with a strong poleward
282   decrease in midlatitudes (between around 20 to 60°), which were found in previous studies on
283   large-scale distribution of d-excess in vapor (Thurnherr et al., 2020;Benetti et al., 2017) and
284   precipitation (Risi et al., 2013a;Terzer-Wassmuth et al., 2021;Pfahl and Sodemann,
285   2014;Bowen and Revenaugh, 2003), based on both observations and modelling.
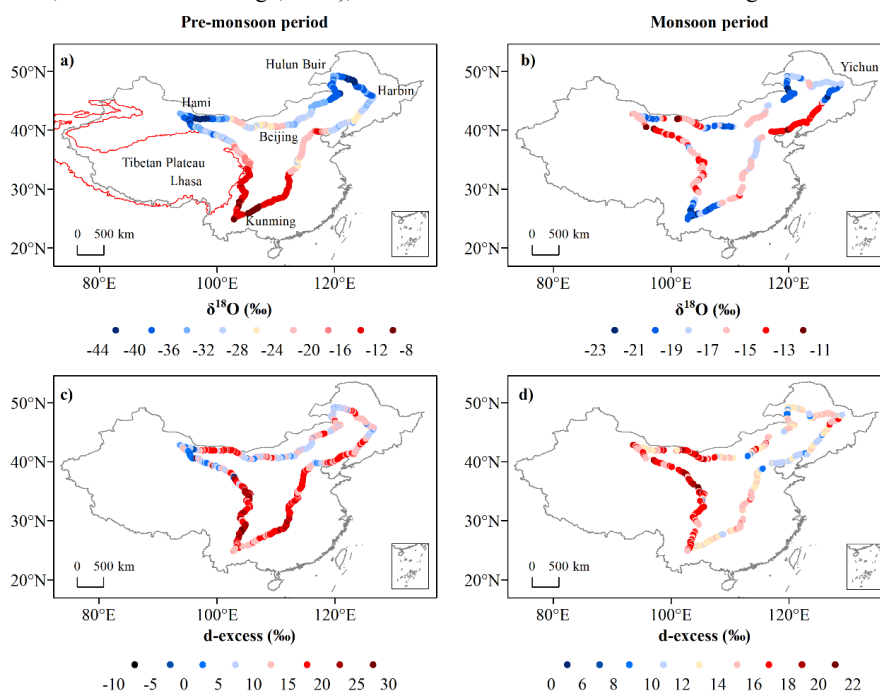

287   Fig.3. Spatial distribution of vapor δ^{18}O (a, b) and d-excess (c, d) during the pre-
288   monsoon period (the left panel) and monsoon period (the right panel).

290   During the monsoon period, the lowest values of vapor δ^{18}O are found in southwestern
291   and northeastern China, with a range of -23‰ to -19‰ (Fig.3b). Higher vapor δ^{18}O values up
292   to -11‰ are founded in central China. The vapor d-excess values (Fig.3d) in western and
293   northwestern China (91°E-109°E, 24°N-43°N) are roughly between 16 and 22‰, higher than
294   in eastern China (mostly between 0 and 16‰).
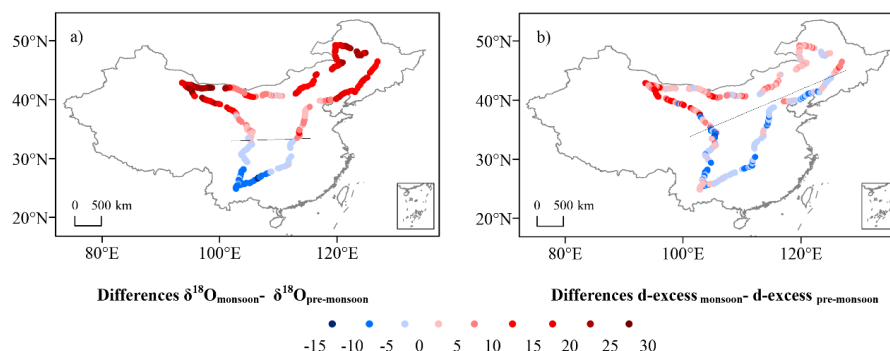
295   3.2 Seasonal variations

Differences $\delta^{18}O_{monsoon}$ - $\delta^{18}O_{pre-monsoon}$ Differences d-excess $_{monsoon}$ - d-excess $_{pre-monsoon}$

-15 -10 -5   0   5   10 15 20 25 30

296

297   Fig.4 Spatial distribution of the isotope differences ($\delta^{18}O_{monsoon}$ - $\delta^{18}O_{pre-monsoon}$ (a) and d-
298   excess$_{monsoon}$ - d-excess$_{pre-monsoon}$ (b)) for the observation locations. The solid black lines separate
299   the areas of positive and negative values of the differences.

300

301   The climate in China features strong seasonality and it is captured in the snapshots of vapor
302   isotopes (Fig.4). Since the observation routes of the two surveys are almost identical, we make
303   a seasonal comparison of the observed vapor isotopes during the two surveys. The lines are
304   drawn to distinguish between positive and negative values of seasonal isotopic differences. The
305   seasonal differences $\delta^{18}O_{monsoon}$ - $\delta^{18}O_{pre-monsoon}$ (Fig.4a) show opposite sign in northern and
306   southern China. In northern China, water vapor $\delta^{18}O$ values are higher during the monsoon
307   period than during the pre-monsoon period, while the opposite are true in southern China. The
308   boundary is located around 35 °N. The largest seasonal contrasts occur in southwest, northwest
309   and northeast China, with seasonal $\delta^{18}O$ differences of -15 ‰, 30 ‰, and 30 ‰, respectively.
310   We also find a spatial pattern of vapor d-excess seasonality (Fig.4b), the separation line of
311   the seasonal variation of d-excess coincides with the 120 mm temporal-mean precipitation (the
312   average for the sampling dates of 2018) line (Fig.S2 f). In southeastern China, the water vapor
313   d-excess is lower during the monsoon period than during the pre-monsoon period. The pattern
314   of seasonal water vapor d-excess in northwestern China is the opposite. The two boundary lines
315   separating the seasonal variations of $\delta^{18}O$ and d-excess do not overlap, suggesting different
316   controls on water vapor $\delta^{18}O$ and d-excess.

317   3.3 Geographical origin of the air masses

318   The vapor isotope composition is a combined result of moisture source (Tian et al.,
319   2007;Araguás-Araguás et al., 1998), condensation and mixing processes along the moisture
320   transport route (Galewsky et al., 2016). To interpret the observed spatial-temporal distribution
321   of vapor isotopes, we start with a diagnosis of the geographical origin of the air masses and
322   then analyze the processes along the back-trajectories. Based on the tracing results from
323   HYSPLIT4 model, we speculate on the potential water vapor sources (Fig.5 and Fig.10):
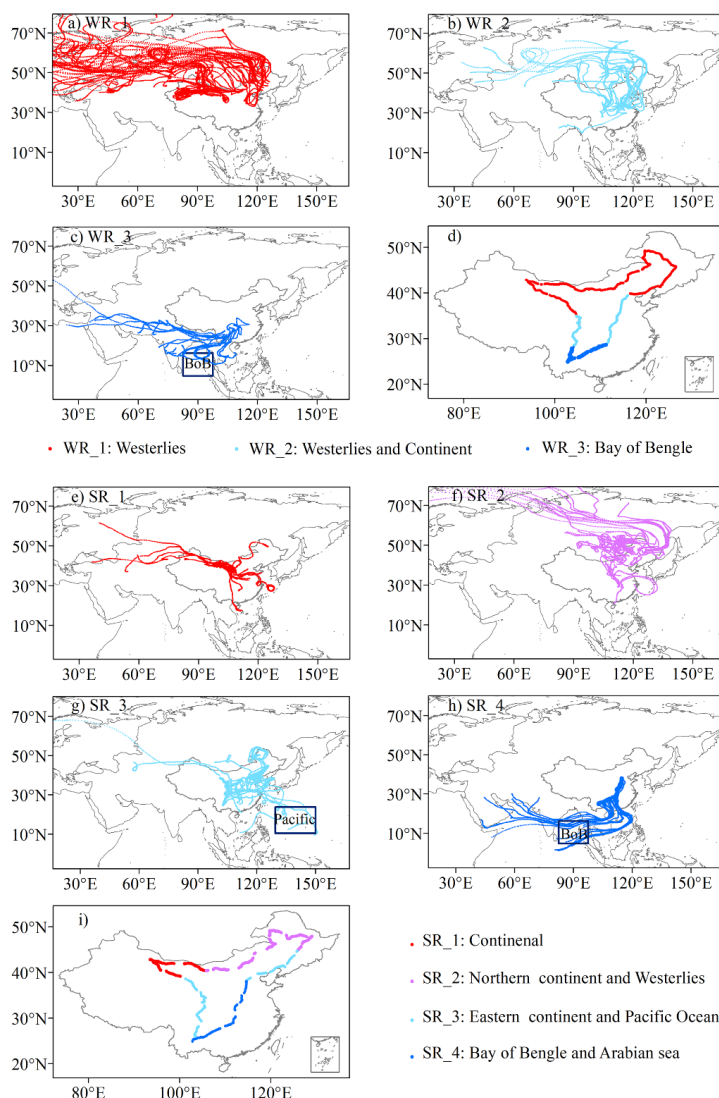
Fig.5 The backward trajectory results (a, b and c for the pre-monsoon period, and e, f, g and h for the monsoon period) and the dividing of the study zones based on geographical origin of the air masses (d for the pre-monsoon period and i for the monsoon period). Note: BoB is the abbreviation for the Bay of Bengal.

During the pre-monsoon period, we categorize our domain into 3 regions (Table 1).

(1) In northern China (WR_1), the air is mainly advected by the Westerlies.

(2) In central China (WR_2), the air also comes from the Westerlies but with a slower wind speed (as shown by the shorter trajectories in 10 days), suggesting potential for greater interaction with the land surface and more continental recycling as moisture source.

(3) In southern China (WR_3), trajectories come from the Southwest and South with

336   marine moisture sources from the Bay of Bengal (BoB).

337   During the monsoon period, we categorize our domain into 4 regions (Table 1):

338   (1) In northwestern China (SR_1), most air masses also spend considerable time over the

339   continent, suggesting some of the vapor can be recycled by continental recycling.

340   (2) In northeastern China (SR_2), trajectories mainly come from the North and though the

341   Westerlies.

342   (3) In central China (SR_3), both in its eastern (from Beijing to Harbin) and western part,

343   trajectories mainly come from the East. This suggests that vapor mainly comes from the Pacific

344   Ocean, or from continental recycling over eastern and central China.

345   (4) In southeastern China (SR_4), trajectories come from the South, suggesting marine

346   moisture sources from the Arabian Sea and the BoB.

347

348   Table 1. The dividing of the study zones based on moisture sources and corresponding

349   vapor δ^{18}O-δ^2H relationship

Pre-monsoon period			
	Water sources (Fig.5)	Region (China)	Climate background	δ^{18}O-δ^2H relationship
WR_1	Westerlies	The north	Westerlies domain	δ^{18}O=8.04δ^2H+12.00 (r^2=0.99, n=750, q<0.01)
WR_2	Westerlies and Continent	The middle	Transition domain	δ^{18}O=8.26δ^2H+23.15 (r^2=0.99, n=281, q<0.01)
WR_3	Bay of Bengal (BoB)	The south	Monsoon domain	δ^{18}O=7.98δ^2H+17.13 (r^2=0.94, n=158, q<0.01)
Monsoon period			
	Water sources (Fig.5)	Region (China)	Climate background	δ^{18}O-δ^2H relationship
SR_1	Continent	The northwest	Transition domain	δ^{18}O=8.31δ^2H+20.92 (r^2=0.99, n=200, q<0.01)
SR_2	Northern continent & Westerlies	The northeast	Transition domain	δ^{18}O=7.53δ^2H+5.13 (r^2=0.98, n=294, q<0.01)
SR_3	Eastern continent & Pacific Ocean	The middle and west	Transition domain	δ^{18}O=7.49δ^2H+7.09 (r^2=0.97, n=271, q<0.01)
SR_4	BoB & Arabian sea	The southeast	Monsoon domain	δ^{18}O=8.21δ^2H+17.81 (r^2=0.99, n=195, q<0.01)

350

351   **4. Discussion**

352   To interpret the spatial and seasonal variations observed both across China and in each

353   region defined in section 3.3, we investigate q–δ diagrams (section 4.1), δ^{18}O-δ^2H relationships

354   (section 4.2), relationships with meteorological conditions at the local and regional scale

355   (sections 4.3 and 4.4) and the impact of air mass origin (section 4.5). We compare our

356   observations with a simulation by a general circulation model Iso-GSM (section 4.6) and use

357   such simulations to estimate the relative contributions of synoptic-scale perturbations and

358   seasonal-mean spatial distribution (section 4.7).
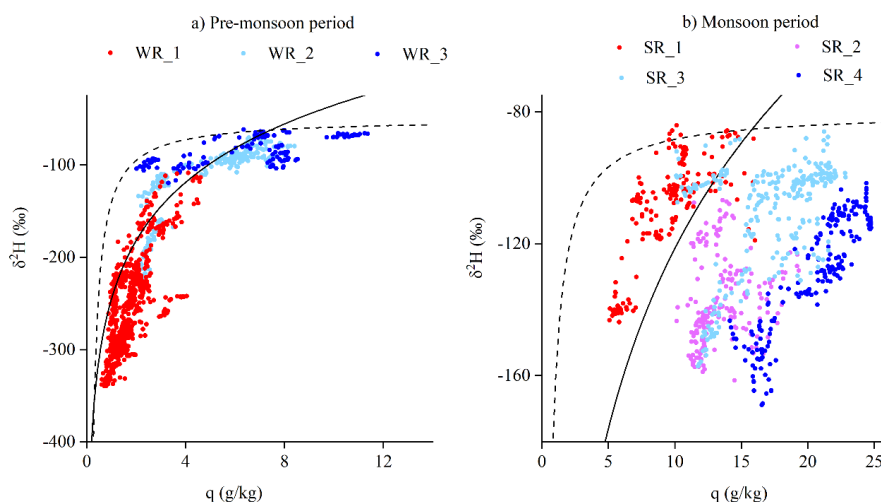
359   4.1 q–δ diagrams

360

361   Fig.6 Scatterplot of observed vapor δ^2H (‰) versus specific humidity q (g/kg) during the pre-
362   monsoon period (a) and monsoon (b) period. The solid black curves show the Rayleigh
363   distillation line calculate for the initial conditions of δ^2H_0 = -50‰, T=15 °C during the pre-
364   monsoon period and δ^2H_0 = -80‰, T=25 °C during the monsoon period. The mixing lines
365   (dashed black curves) are calculated using a dry end-member with q = 0.2 g/kg and $\delta^2H = -$
366   500 ‰ and air parcels for the corresponding Rayleigh curve as a wet end-member.

367

368   The progressive condensation of water vapor from an air parcel from the source region to
369   the sampling site and the subsequent removal of condensate results in a gradual reduction of
370   vapor isotope ratios. This relationship can be visualized in a q–δ diagram, which has been used
371   in many studies of the vapor isotopic composition (Noone and David, 2012;Galewsky et al.,
372   2016). Observations along the Rayleigh distillation line indicate progressive dehydration by
373   condensation. Observations above the Rayleigh line indicate either mixing between air masses
374   of contrasting humidity (Galewsky and Hurley, 2010) or evapotranspiration (Galewsky et al.,
375   2011;Samuels-Crow et al., 2015;Noone and David, 2012;Worden et al., 2007). Observations
376   below the Rayleigh line indicate the influence of rain evaporation (Noone and David,
377   2012;Worden et al., 2007). Figure 6 shows the observed vapor q–δ^2H for different regions
378   during the pre-monsoon (a) and monsoon (b) period. This figure will be interpreted in the light
379   of meteorological variables along back-trajectories (Fig.10).
380   During the pre-monsoon period, most q-δ^2H measurements are located surrounding or
381   overlapping the Rayleigh curve (the solid black curve in Fig.6a). Therefore, the observed spatial
382   pattern can mostly be explained by the gradual depletion of vapor isotopes by condensation.
383   The data for the three moisture sources are distributed in different positions of the Rayleigh
384   curve, relate to different moisture origins or different original vapor isotope values. This is
385   confirmed by the back-trajectory analysis: the Westerlies bring cold and dry air to northern
386   China (WR_1, Fig.5a, Fig.10a and c), consistent with the vapor further along the Rayleigh
387   distillation, and thus very depleted (Fig.3a). The relatively high T and q along the ocean-sourced

388   air trajectory reaching southern China (WR_3, Fig.5c, Fig.10a and c) is consistent with an early
389   Rayleigh distillation phase during moisture transport, and thus higher water vapor $\delta^{18}O$ in
390   southern China (Fig.3a). Some observations in the WR_3 region (Fig.5c) are located below the
391   q-δ^2H Rayleigh distillation curve, indicating the influence of rain evaporation (Noone and
392   David, 2012;Worden et al., 2007). This is consistent with the fact that air originates from the
393   BoB, where deep convection begins to be active, and thus rain evaporation become a source of
394   water vapor.
395   During the monsoon period, we find a scattered relationship in the q–δ^2H diagram for
396   different regions, implying different moisture sources and/or water recycling patterns during
397   moisture transport. Data measured in the SR_1 region (Fig.5i) fall above the Rayleigh
398   distillation line (solid black curve in Fig.6b), likely due to the presence of moisture originating
399   from continental recycling. A larger number of q-δ^2H measurements (most of the measurements
400   from the SR_2, SR_3, and SR_4 regions, Fig.5i) are located below the Rayleigh curve,
401   indicating moisture originating from the evaporation of rain drops within and below convective
402   systems (Noone and David, 2012;Worden et al., 2007). In SR_3 and SR_4 regions, this is
403   consistent with the high precipitation rate along Southerly and Easterly back-trajectories
404   (Fig.10f). The convection is active over the Bay of Bengal, Pacific Ocean and South-Eastern
405   Asia, as shown by the low OLR (<240W/m 2) in these regions (Fig.S3) (Wang and Xu, 1997).
406   Therefore, a significant fraction of the water vapor originates from the evaporation of rain drops
407   in convective systems. These results support recent studies showing that convective activity
408   depleted the vapor during transport by the Indian and East Asian monsoon flow (Cai et al.,
409   2018;He et al., 2015;Gao et al., 2013). In SR_2 region, the relatively low water vapor $\delta^{18}O$,
410   below the Rayleigh curve, is also probably associated with the evaporation of rain drop under
411   deep convective systems. This is confirmed by the high precipitation rates along Northerly
412   back-trajectories (Fig.10f), reflecting summer continental convection.
413   In northern China, q–δ diagrams show stronger distillation during the pre-monsoon period.
414   This suggests a "temperature dominated" control. Very low regional T during the pre-monsoon
415   period (Fig.S2 a and Fig.10a) are associated with low saturation vapor pressures and enhanced
416   distillation, producing lower vapor $\delta^{18}O$. The T in summer is higher (Fig.S2 b and Fig.10b),
417   allowing for higher vapor $\delta^{18}O$. The $\delta^{18}O_{monsoon}$ - $\delta^{18}O_{pre-monsoon}$ values in this region are therefore
418   positive (Fig.4a). In the South, q–δ diagrams suggest the stronger influence of rain evaporation
419   during the monsoon period. Higher precipitation amount significantly reduce $\delta^{18}O$ in the South
420   (Fig.10f), even though T was higher during the monsoon period than in pre-monsoon. This
421   suggests a "precipitation dominated" control in this region, explaining the negative values of
422    $\delta^{18}O_{monsoon}$ - $\delta^{18}O_{pre-monsoon}$. This seasonal pattern in $\delta^{18}O$ is consistent with the results in
423   precipitation isotopes (Araguás-Araguás et al., 1998;Wang and Wang, 2001). The boundary line
424   separating the seasonal variations of $\delta^{18}O$ is also consistent with previous study on seasonal
425   difference in vapor δ^2H retrieved by TES and GOSAT (Shi et al., 2020).

426   4.2 The $\delta^{18}O$-δ^2H relationship
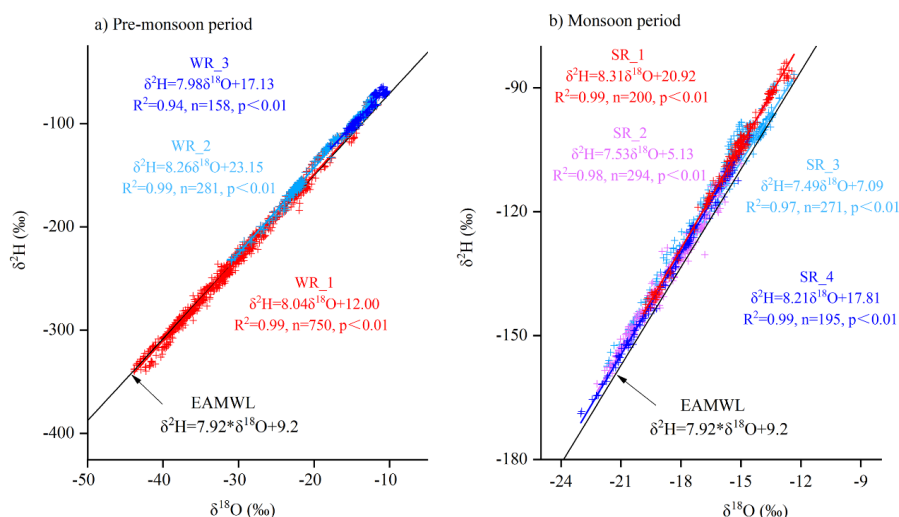
Fig.7 Regional patterns of vapor $\delta^{18}O$ - δ^2H relation during pre-monsoon period (a) and monsoon (b) period, compared with the East Asia Meteoric Water Line (EAMWL) (Araguás-Araguás et al., 1998).

The $\delta^{18}O$-δ^2H relationship is usually applied to diagnose the moisture source and water cycling processes related to evaporation. Figure 7 and Table 1 show the $\delta^{18}O$-δ^2H relationship for different regions in the two seasons. We also plot the East Asian Meteoric Water Line (EAMWL) for a reference. Vapor $\delta^{18}O$-δ^2H is usually located above Meteoric Water Line owing to the liquid water and vapor fractionation.

During the pre-monsoon period (Fig.7a), the data in northern China (WR_1, Fig.5a) are located at the lower-left area in the $\delta^{18}O$-δ^2H graph, with similar slope and intercept as EAMWL ($\delta^2H = 8.04 \delta^{18}O + 12.00$). This corresponds to air bring by the Westerlies and following Rayleigh distillation. The linear relationship for the vapor in middle China (WR_2, Fig.5b) has the steepest slope and highest intercept ($\delta^2H = 8.26\delta^{18}O + 23.15$). These properties are associated with a strong d-excess, consistent with strong continental recycling. As continental recycling is known to have an enriching effect on the water vapor (Salati et al., 1979) and be associated with high d-excess (Gat and Matsui, 1991;Winnick et al., 2014). The high intercept is further consistent with a correlation between $\delta^{18}O$ and d-excess, which can typically result from continental recycling (Putman et al., 2019). The data for vapor originating from the BoB (WR_3, Fig.5c) are located to the upper right of the EAMWL. Their regression correlation shows similar features ($\delta^2H = 7.98 \delta^{18}O + 17.13$) to that of the monsoon season (with a slope of 8.21 and an intercept of 17.81). We find similar atmospheric conditions in the BoB (with the region marked as rectangle in Fig.5c and h) during the two observation periods, with T=26℃ and RH=76% during pre-monsoon period and T=28℃ and RH=78% during the monsoon period, suggesting that the BoB source may have similar signals on vapor $\delta^{18}O$ and δ^2H in both seasons. These observed vapor $\delta^{18}O$-δ^2H patterns are consistent with the back-trajectory results

454   indicating that the Westerlies persist in northern China during the pre-monsoon period, while

455   moisture from the BoB has already reached southern China.

456   During the monsoon period (Fig.7b), the data in northwestern China (SR_1, Fig.5e) with

457   continental moisture sources is located in the upper right of the graph but above the EAMWL,

458   with a steepest slope and highest intercept for the linear $\delta^{18}O$-δ^2H relationship ($\delta^2H = 8.31\delta^{18}O$

459   +20.92). In contrast, the observations in southeastern China with BoB sources (SR_4, Fig.5h)

460   are located in the lower left of the graph, with relatively lower intercept ($\delta^2H = 8.21\delta^{18}O$

461   +17.81). This is the opposite pattern compared to the pre-monsoon season. The observations

462   from the SR_3 region (Fig.5g) also have a low slope and low intercept ($\delta^2H = 7.49 \delta^{18}O$ +7.09).

463   This is consistent with the oceanic moisture from the Pacific Ocean. Also, these $\delta^{18}O$-δ^2H data

464   are located in the upper right of the graph with more scattered relation (with the lowest

465   correlation coefficient), suggesting more diverse moisture sources. This is consistent with the

466   mixing of water vapor from continental recycling and Pacific Ocean (Fig.5g). The observations

467   in northeastern China (SR_2, Fig.5f) are located at the lower left of the graph, suggesting the

468   influence of condensation along trajectories in northern Asia (Fig.10f). Compared to the SR_3

469   and SR_4 regions, the slope and intercept of the observations in SR_2 region are lower ($\delta^2H =$

470      $7.53\delta^{18}O$ +5.13), reflecting different origins of moisture.

471   4.3 Relationship with local meteorological variables
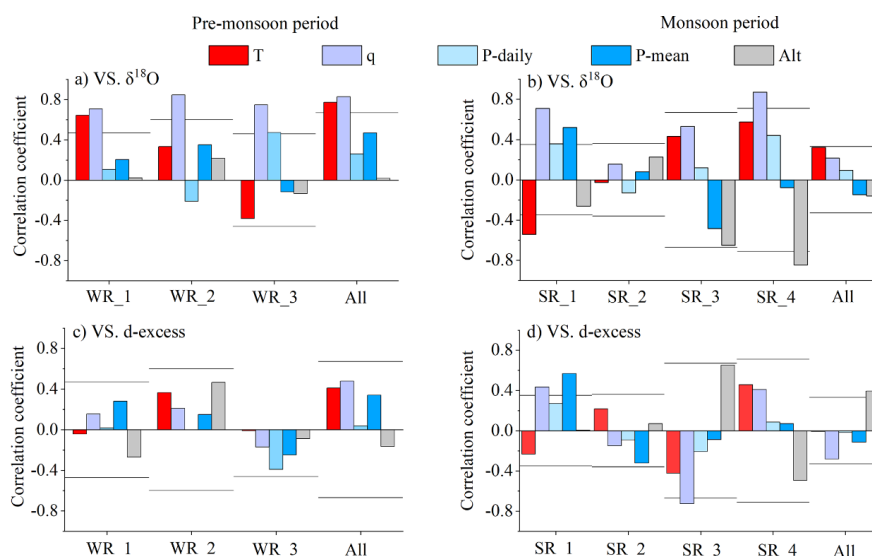
473 Fig.8 Regional patterns of the correlation between $\delta^{18}O$ (a, b), d-excess (c, d) and various local

474 factors (temperature (T), specific humidity (q), daily precipitation amount (P-daily) and

475 temporal-mean precipitation amount for the sampling dates (P-mean), and altitude (Alt)). The

476 left panel is for the pre-monsoon period and the right is for the monsoon period. Horizontal

477 lines indicate the correlation threshold for statistical significance (p<0.05), considered the

478 degree of freedom.

479

480   Here we analyze the relationship between vapor $\delta^{18}O$, d-excess and local meteorological

481 parameters, for all observations, and separately for the different regions (Fig.8 and Table S1).

482   We have taken particular care to estimate the statistical significance of the correlation
483 coefficients. The statistical significance of a correlation depends on the correlation coefficient
484 and on the degree of freedom D of the observed $\delta^{18}O$ and d-excess time series. Since these
485 variables evolve smoothly in time and are sampled at a high frequency, the total number of
486 samples overestimates the degree of freedom D of the time series. We thus estimated the degree
487 of freedom D as $Ţ/\eta$, where $Ţ$ is the length of the sampling period and η is the characteristic
488 auto-correlation time scale of the time series (an example of this calculation is given in III.
489 Supplementary text). A similar method was used to calculate the degree of freedom of the signal
490 in Roca et al.(2010). Table S2 summarizes the threshold for the correlation coefficient to be
491 statistically significant at 95%, for the two seasons, the different regions and the variable of
492 interest.

493   During the pre-monsoon period, all observations exhibit a "temperature effect" (Fig.8a),
494 with significant and positive correlation between $\delta^{18}O$ and T (r = 0.77, p<0.05, Table S1). This
495 results from the high correlation between $\delta^{18}O$ and q (r = 0.83, p<0.05, Table S1), consistent
496 with the Rayleigh distillation, and between T and q (r = 0.54, p<0.05), consistent with the
497 Clausius Clapeyron relationship. The vapor $\delta^{18}O$ in the WR_1 (Fig.5a) region show similar
498 correlations with T and q as for all observations. Rayleigh distillation thus contributes to the
499 relationship between $\delta^{18}O$ and T observed in northern China. In contrast, no significant positive
500 correlation between vapor $\delta^{18}O$ and T is observed in the WR_3 region with the BoB water
501 source. This is consistent with the fact that the moisture from the BoB has already influence
502 southern China during the pre-monsoon period (Fig.5c). The weak positive correlation in most
503 regions between $\delta^{18}O$ and P-daily and P-mean might simply reflect the control of q on observed
504 vapor $\delta^{18}O$, due to the relatively high correlation between observed P-mean and q, with r = 0.58
505 for all observations (Fig.2).

506   During the monsoon period (Fig 8b), no significant correlation emerges when considering
507 all observations. Vapor $\delta^{18}O$ is still significantly correlated with q in the SR_1 (Fig.5e, r = 0.71,
508 p<0.05, Table S1) and SR_4 (Fig.5h, r = 0.87, p<0.05, Table S1) regions. This is consistent
509 with different degrees along the Rayleigh distillation. The absence of correlation with T
510 suggests that the variations in q mainly reflect variations in relative humidity that are associated
511 with different air mass origins. The $\delta^{18}O$ is significantly anti-correlated with Alt in the SR_4
512 region (r = -0.85, p<0.05, Table S1), consistent with the "altitude effect" in precipitation and
513 water vapor (Dansgaard, 1964;Galewsky et al., 2016).

514   The vapor d-excess for all observations during the monsoon period (Fig.8d) is positively
515 correlated with Alt (r = 0.39, p<0.05, Table S1). One possible reason is that the vapor d-excess
516 is lower in coastal areas at lower altitudes, while at higher altitudes in the west, more recycling
517 moisture leads to higher d-excess. Alternatively, this may reflect the fact that the d-excess
518 generally increases with altitude (Galewsky et al., 2016). In the SR_1 region (Fig.5e), in arid
519 northwestern China, vapor d-excess is positively correlated with q (r = 0.43, p<0.05, Table S1)
520 and P-mean (r = 0.57, p<0.05, Table S1) during the monsoon period, suggesting that rain
521 evaporation may also contribute to high d-excess (Kong and Pang, 2016). Other than these
522 examples, the correlation coefficients between the d-excess and T, q, P, and Alt are not
523 significant (Fig.8c and d), indicating that the local meteorological variables are not strongly
524 related to vapor d-excess, as was reported in previous studies for precipitation isotopes (Guo et

525   al., 2017;Tian et al., 2003).

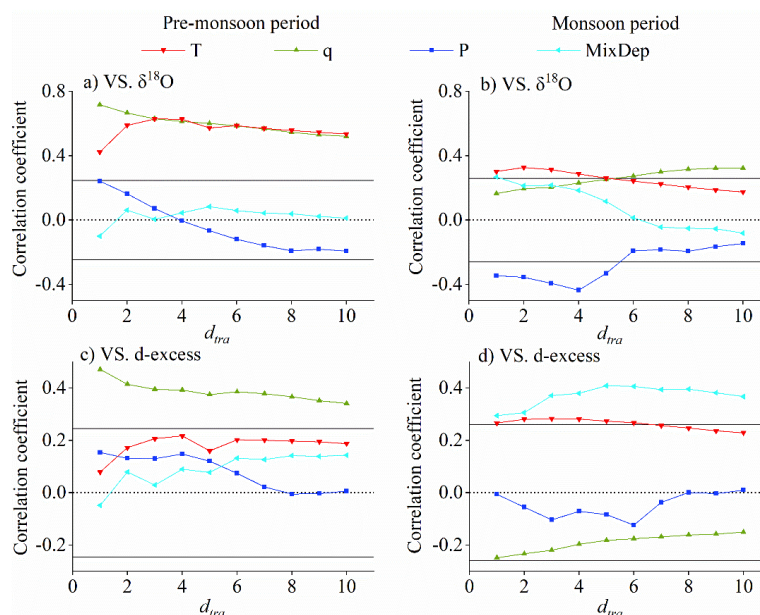526   4.4 Relationship with meteorological variables along trajectories

527

528   Fig.9 Correlation between $\delta^{18}O$ (a, b), d-excess (c, d)), and various meteorological factors (air
529   temperature (T), specific humidity (q), precipitation (P), and mixing depth (MixDep)) along the
530   air mass trajectories during the pre-monsoon period (the left panel) and monsoon period (the
531   right panel). The coordinate dtra represents the period prior to the observations (1~10 days),
532   e.g., dtra=2, 3, 4…… represents the correlation coefficient with the temporal mean of
533   meteorological data on the air mass trajectories during vapor transmission from the 1st to the
534   2nd, 3rd, 4th …… day prior to the observations. Horizontal solid lines indicate the correlation
535   threshold for statistical significance ($p<0.05$).

536

537   Vapor isotopes values also reflect processes that occur along air mass trajectories. We
538   therefore perform a correlation analysis between vapor isotope observations and the temporal
539   mean meteorological conditions along air mass trajectories. The meteorological conditions are
540   averaged over the *dtra* previous days (1~10 days) prior to the observations.
541   The $\delta^{18}O$ values have the strongest correlations with T and q along air mass trajectories
542   during the pre-monsoon period (Fig.9a). The results show gradually increasing positive
543   correlation coefficients as dtra changes from 10 to 3, reflecting the large spatial and temporal
544   coherence of T variations during the pre-monsoon period. During the monsoon period, the
545   negative correlation coefficients between $\delta^{18}O$ and P (Fig.9b) become more significant as *dtra*
546   increases from 1 to 4 and less significant as *dtra* increases from 5 to 10. This result indicates a
547   maximum impact of P during a few days prior to the observations, as observed also for
548   precipitation isotopes (Gao et al., 2013;Risi et al., 2008a). It is further consistent with the
549   influence of precipitation along back-trajectories (Fig.10f). Mixing depth (MixDep) is stably

550 and positively correlated with d-excess. A hypothesis to explain this correlation is that when
551 the MixDep is higher, stronger vertical mixing of convective system transports vapor with
552 higher d-excess values from higher altitude to the surface (Galewsky et al., 2016;Salmon et al.,
553 2019).

554 4.5 Relationship between water vapor isotopes and moisture sources

555   In section 4.1 to 4.4, we have discussed that different moisture sources and corresponding
556 processes on transport pathways are related to the observed spatial patterns both in vapor $\delta^{18}O$
557 and d-excess.
558   We also identify different isotopic values of vapor from different ocean sources during the
559 monsoon period. The vapor $\delta^{18}O$ in the zone from Beijing to Harbin and western China with
560 Pacific Ocean and continental origins (SR_3 region, about -17‰ to -13‰) are higher than those
561 in the Southeast with BoB sources (SR_4 region, about -23‰ to -15‰) (Fig.5i and Fig.3b). In
562 sections 4.1 and 4.2, we have shown that it is related to the extent of the Rayleigh distillation
563 and rain evaporation associated with convection along trajectories. Earlier studies suggest that
564 lower $\delta^{18}O$ values were observed from the Indian monsoon source than from Pacific Asian
565 monsoon moisture due to the different original isotope values in the source regions (Araguás-
566 Araguás et al., 1998). To better isolate the direct effect of moisture sources, we extract the initial
567 vapor isotopes of the Indian and East Asian monsoon systems (the regions are marked as
568 annotated rectangles in Fig.5g and h) for the sampling dates of 2018 from the Iso-GSM model.
569 The values are about $\delta^{18}O$=-12‰ and $\delta^{2}H$ =-83‰ in the northern BoB and $\delta^{18}O$ =-14‰ and
570 $\delta^{2}H$ =-97‰ in the eastern Pacific Ocean. The initial vapor isotope values of the two vapor
571 sources are not significantly different. The initial vapor isotopes in the BoB are even slightly
572 higher than those in the Pacific Ocean, contrary to moisture source hypothesis. The OLR was
573 significantly lower in the BoB than in the Pacific Ocean (Fig.S3). This suggests that the more
574 active convection in the Indian Ocean leads to lower water vapor isotope ratios (Liebmann and
575 Smith, 1996;Bony et al., 2008;Risi et al., 2008b;Risi et al., 2008a) in southeastern China, rather
576 than the initial composition of the moisture source.
577   Continental recycling probably also contribute to higher $\delta^{18}O$ in the SR_3 region (Fig.5i
578 and Fig.3b) (Salati et al., 1979), especially in western China (Fig.5i), which can be confirmed
579 by the higher d-excess in this region (Fig.3d) (Gat and Matsui, 1991;Winnick et al., 2014). In
580 the zone from Beijing to Harbin (Fig.5i), greater proportion of water vapor from Pacific sources
581 than continental recycling and is in the early stage of Rayleigh distillation, could result in high
582 vapor $\delta^{18}O$ (Fig.3b) but relatively low d-excess (Fig.3d).
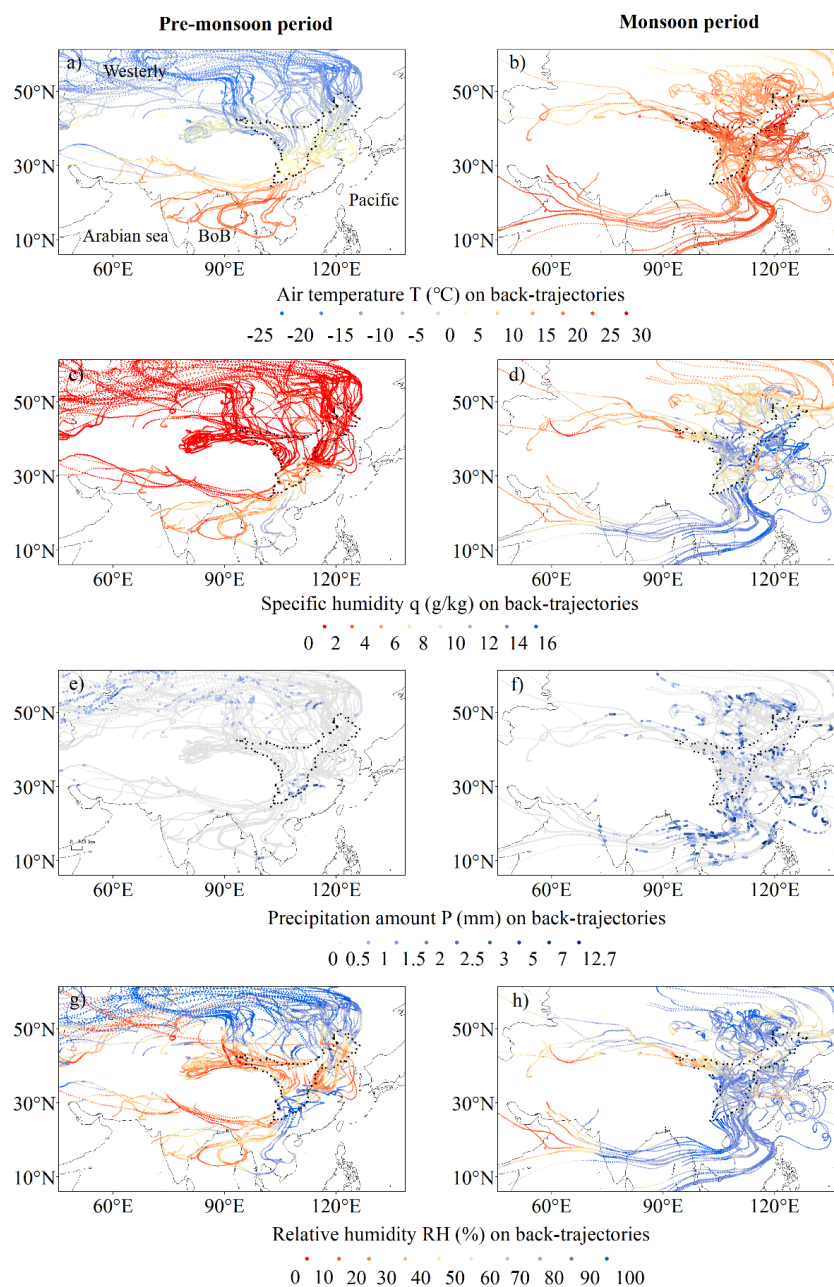
583
584 Fig.10 Meteorological conditions simulated by HYSPLIT4 model along the 10-day air back-
585 trajectories for the on-route sampling positions during the two surveys: (a, b) air temperature T
586 (℃), (c, d) specific humidity q (g/kg), (e, f) precipitation amount P (mm) and (g, h) relative
587 humidity RH (%). The left panel is for the pre-monsoon period and the right is for the monsoon
588 period. The driving locations and time every 2 hours are used as starting points. Note: BoB is
589 the abbreviation for the Bay of Bengal.

590   In previous studies, the d-excess has been interpreted as reflecting the moisture source and
591 evaporation conditions (Jouzel et al., 1997). During the pre-monsoon period, lower T and higher
592 RH over evaporative regions for the vapor transported by the Westerlies (Fig.10 a and g, Fig.S2
593 a and g) reduces the kinetic fractionation and produces lower vapor d-excess in the WR_1
594 region (Fig.5a, Fig.3c) (Jouzel et al., 1997;Merlivat and Jouzel, 1979). In contrast, higher T and
595 lower RH over evaporative regions (Fig.10 a and g, Fig.S2 a and g) for the vapor coming from
596 the South leads to higher d-excess in southern China (WR_3, Fig.5c, Fig.3c). This is consistent
597 with the global-scale poleward decrease in T and increase in surface RH over the oceans
598 resulting in global-scale poleward decrease in d-excess at mid-latitudes (Risi et al.,
599 2013a;Bowen and Revenaugh, 2003). We find that continental recycling further increases d-
600 excess in middle China (WR_2, Fig.5b, Fig.3c) (Gat and Matsui, 1991;Winnick et al., 2014).
601 During the monsoon period, the lower vapor d-excess observed in eastern China (Fig.3d) is
602 likely a sign of the oceanic moisture, derived from source regions where RH at the surface is
603 high (Fig.10h and Fig.S2 h) and thus reduce kinetic fractionation and lower d-excess. The high
604 d-excess values observed in western and northwestern China (Fig.3d) reflect the influence of
605 continental recycling (Fig.5e and g).

606   The seasonal variation of moisture sources also results in a seasonal difference in d-excess
607 (Fig.4b). In southeastern China, RH over the ocean surface in summer is higher than in winter
608 (Fig.S2 g and h, and Fig.10g and h), resulting in negative values of d-excess$_{monsoon}$ - d-excess$_{pre-}$
609 $_{monsoon}$ (Fig.4b). Northwestern China has an opposite pattern of seasonal vapor d-excess. This
610 result largely due to the extremely low vapor d-excess during the pre-monsoon period (Fig.3c).
611 Also, we speculate that a greater contribution of continental recycling leads to higher d-excess
612 during the monsoon period than during the pre-monsoon period (Risi et al., 2013b) and the
613 positive values of the d-excess$_{monsoon}$ d-excess$_{pre-monsoon}$ (Fig.4b).

614 4.6 Evaluation of Iso-GSM simulations

615   Our observed variations along the routes across China for a given period represent a
616 mixture of synoptic-scale perturbations and seasonal-mean spatial distribution. To quantify
617 these relative contributions, we use daily and temporal-mean simulations of Iso-GSM.

618   Before using the simulations, we first evaluate the ability of Iso-GSM to capture the
619 observed spatial-temporal vapor isotopic variations in China here.

620   Figure 11 shows the comparison of the measured vapor $\delta^{18}O$ and the outputs of Iso-GSM.
621 Iso-GSM captures the variations in observed vapor $\delta^{18}O$ well during the pre-monsoon period,
622 with correlation coefficient of r = 0.84 (p<0.01) (Table S3). The simulation results during the
623 monsoon period are roughly in the range of observations, but detailed fluctuations are not well
624 captured, with r = 0.24 (p>0.05) (Table S3). The largest differences occur in the SR_1 zone.

625   To diagnose the reasons for the GCMs performance, we compare the observed and
626 simulated vapor $\delta^{18}O$, q, P-mean and T (spatial variations of the differences are shown in Figure
627 12, time series of the differences are shown in Figure S4, and correlation coefficients are shown
628 in Table S3). During the pre-monsoon period, Iso-GSM overestimates observed $\delta^{18}O$ along
629 most of the survey route (Fig.12a), with the largest difference in northwestern China, and
630 underestimates the vapor $\delta^{18}O$ in the southern part of the study region. Our results are consistent
631 with previous studies showing that many models underestimate the heavy isotope depletion in
632 pre-monsoon seasons in subtropical and mid-latitudes, especially in very dry regions (Risi et

633 al., 2012). The differences in $\delta^{18}O$ (Fig.12a) and q (Fig.12c) are spatially consistent. The
634 overestimation (respectively underestimation) of $\delta^{18}O$ therefore could be due to the
635 overestimation (respectively underestimation) of q. The contrasting errors in southern and
636 northern China also probably suggest that Iso-GSM does not capture the influence of BoB
637 moisture on southern region during the pre-monsoon period well. Despite this, the good
638 agreement during pre-monsoon period is probably due to the dominant control by Rayleigh
639 distillation on spatial variations of isotopes in this season. The q variation, in relation with T,
640 drives vapor isotope variations and is well captured by Iso-GSM spatially, with significant
641 correlations between observed and simulated q (r = 0.84, slope=0.70 in Table S3) and T (r =
642 0.87, slope=0.70 in Table S3), though q is overestimated in the North and underestimated in the
643 South.

644 　　During the monsoon period, Iso-GSM underestimates the vapor $\delta^{18}O$ along most of the
645 survey route (Fig.12b). It is possible that Iso-GSM generally overestimates the influence of the
646 monsoon that depletes vapor, or underestimates the enriching effect of continental recycling. In
647 particular, Iso-GSM underestimates q and T along most of the survey route (Fig.12 d and h, and
648 Fig.S4), and overestimates P-mean in the South (Fig.12f). Besides, the altitude effect is wrongly
649 simulated for several regions with higher correlations (Fig.S5), which could also result in
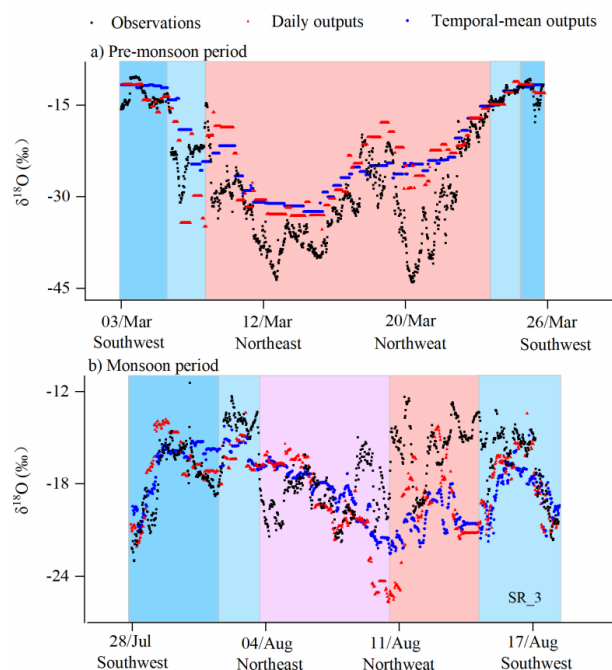650 underestimates of $\delta^{18}O$.

651
652 Fig.11 Comparison of observed vapor δ18O (observations) with outputs of Iso-GSM during the
653 pre-monsoon period (a) and monsoon period (b). The model results in this graph are from the
654 daily and temporal-mean surface layer outputs for the sampling dates and locations. Note: the
655 outputs during the monsoon period had been corrected for altitude.
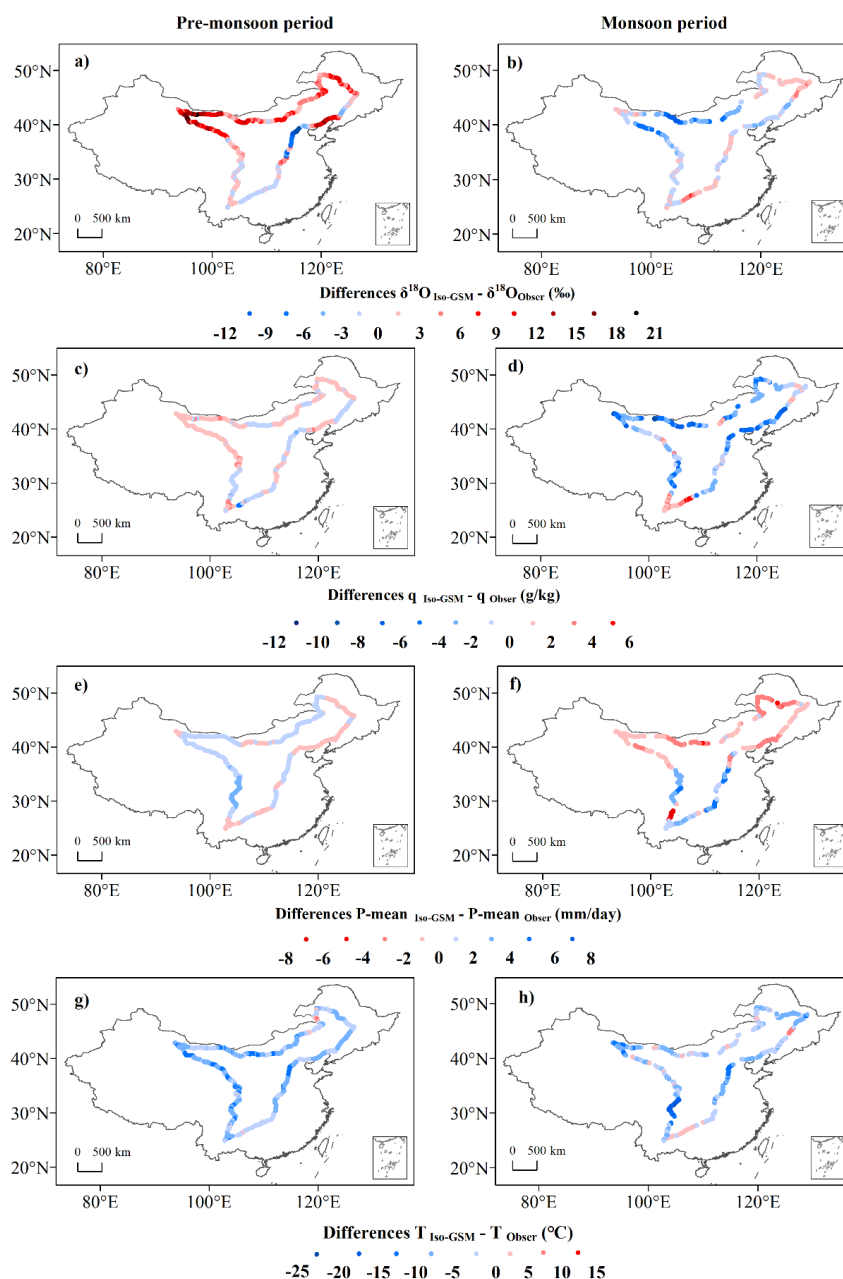
656

657　Fig.12 Spatial distribution of the differences between the outputs of Iso-GSM (subscripts are

658　IsoGSM) and observations (subscripts are Obser) during the pre-monsoon period (the left panel)

659　and monsoon period (the right panel): $\delta^{18}O$ (a and b, ‰), specific humidity q (c and d, g/kg),

660　temporal-mean precipitation amount P-mean for the sampling dates (e and f, mm/day), and

661　temperature T (g and h, °C).

Atmospheric
Chemistry
and Physics
Discussions

662 4.7 Disentangling synoptic and spatial variations using isotope-enabled general circulation
663   models

664   The variations for temporal-mean outputs of $\delta^{18}O$ are smoother but similar to those for the
665 daily outputs from Iso-GSM (Fig.11). The daily variations of $\delta^{18}O$ simulate by Iso-GSM can be
666 written as:
667      $\delta^{18}O\_daily = \delta^{18}O\_seaso + \delta^{18}O\_synoptic$ (4)
668   where $\delta^{18}O\_seaso$ is the temporal-mean $\delta^{18}O$ for the sampling dates and $\delta^{18}O\_synoptic$
669 $= \delta^{18}O\_daily - \delta^{18}O\_seaso$. The first term represents the contribution of seasonal-mean spatial
670 variations, whereas the second term represents the contribution of synoptic scale variations. To
671 evaluate contribution of these two terms, we calculate the slopes of $\delta^{18}O\_daily$ as a function of
672 $\delta^{18}O\_seaso$ ($a_{\_seaso}$), and of $\delta^{18}O\_daily$ as a function of $\delta^{18}O\_synoptic$ ($a_{\_synopic}$). The relative
673 contributions of spatial and synoptic variations correspond to $a_{\_seaso}$ and $a_{\_synopic}$ respectively.
674 The same analysis is done for T, q and P as well (Table 2).

675

676 **Table 2** The relative contribution (in units of 1) of spatial variations at the regional scale for
677   a given season ($a_{\_seaso}$) vs synoptic-scale variations ($a_{\_synopic}$). Notes: we used the simulated
678      $\delta^{18}O$, temperature T, specific humidity q and precipitation P from Iso-GSM. The sum is the
679      $a_{\_seso}$ plus $a_{\_synoptic}$.

		$a_{\_seaso}$	$a_{\_synoptic}$	Sum
Pre-monsoon	$\delta^{18}O$	0.81	0.19	1
	T	0.77	0.23	1
	q	0.93	0.07	1
	P	0.24	0.76	1
Monsoon	$\delta^{18}O$	0.60	0.40	1
	T	0.69	0.31	1
	q	0.86	0.14	1
	P	0.47	0.53	1

680

681   During the pre-monsoon period, the relative impact of seasonal mean spatial variations on
682 the total simulated variations of $\delta^{18}O$ (81%) are much higher than that of synoptic-scale
683 variations (19%), suggesting that the observed variability is mainly due to spatial variability,
684 and marginally due to synoptic-scale variability. During the monsoon period, the relative
685 impact of synoptic-scale variations (40%) on the total simulated variations of $\delta^{18}O$ become
686 more significant, but the contribution of seasonal-mean spatial variations still dominate (60%).
687 The same patterns are observed for T and q in both seasons. In contrast, the contribution of
688 synoptic-scale variations to daily P variations is 76% during the pre-monsoon period and 53%
689 during monsoon period. This is consistent with the local and intermittent nature of precipitation.

690 4.8 Urban emissions

691   We observed abnormally low d-excess in short episodes while vehicles were driving in or
692 out cities or stuck in traffic jams (Fig.2 and Section 2.3). These data have a much lower than
693 normal d-excess, and a much lower intercept in the linear $\delta^{18}O$ - $\delta^{2}H$ relationship (Fig.S6). We

694   argue that these data are significantly influenced by fuel combustion. Previous studies on urban
695   vapor isotopes (Gorski et al., 2015;Fiorella et al., 2018;Fiorella et al., 2019) showed that the
696   vapor d-excess closely tracked changes in CO_2 through inversion events and during the daily
697   cycle dominated by patterns of human activity, and combustion-derived water vapor is
698   characterized by a low d-excess value due to its unique source. We also find that the d-excess
699   values are especially low when the vehicle was in cities in the afternoon. The values increased
700   to normal during the night. This diurnal cycle is likely related to the emission intensity and
701   atmospheric processes (Fiorella et al., 2018). These results imply that the emission of water
702   vapor through the combustion of fossil fuels is a significant component of the atmospheric
703   water budget in the urban boundary layer and a very common phenomenon in most cities. This
704   strong signal is detectable by vapor isotopes and has a significant influence on the vapor d-
705   excess in urban areas and the relationship between $\delta^{18}O$ and δ^2H, with potential implications
706   for urban climate, ecohydrology, and photochemistry (Gorski et al., 2015).

707   **5   Conclusion**

708   Our new, vehicle-based observations document spatial and seasonal variability in surface
709   water vapor isotopic composition across a large part of China. Both during the pre-monsoon
710   and monsoon periods, it is clear that different moisture sources and corresponding processes on
711   transport pathways explain the spatial patterns both in vapor $\delta^{18}O$ and d-excess (summarized in
712   Fig.13):
713   (1) During the pre-monsoon period (Fig.13a), the latitudinal gradient of vapor $\delta^{18}O$ and d-
714   excess were observed. The gradient in $\delta^{18}O$ reflects the "temperature effect", Rayleigh
715   distillation appears to be the dominant control, roughly consistent with earlier studies on
716   precipitation. Vapor in northern China, derived from westerlies, and subject to stronger
717   Rayleigh distillation (low q and T), is characterized by very low isotope ratios. Less complete
718   Rayleigh distillation (relatively high q and T) results in less depleted vapor in southern China.
719   The vapor d-excess in northern China is low, probably due to the high RH over high-latitude
720   oceanic moisture sources for the vapor transported by the Westerlies (green arrow), reducing
721   the kinetic fractionation during ocean evaporation. In contrast, the lower RH over low-latitude
722   moisture sources for the vapor transported to southern China leads to higher d-excess (yellow
723   arrow). Additional vapor sourced from continental recycling (red zigzag arrows), further
724   increases the d-excess values in middle China. This distribution is consistent with the back-
725   trajectory results showing that during the pre-monsoon period, the vapor in southwestern China
726   comes from the BoB, whereas Westerly moisture sources still persist in northern China.
727   (2) During the monsoon period (Fig.13b), the lowest vapor $\delta^{18}O$ occurred in southwestern
728   and northeastern China, and higher vapor $\delta^{18}O$ values were observed in between, while the d-
729   excess features a west-east contrast. The relatively lower vapor $\delta^{18}O$ result from deep
730   convection along the moisture transport pathway. Meanwhile, the mixing with moisture from
731   continental recycling increases the vapor $\delta^{18}O$ values in middle and northwestern China. We
732   observed lower vapor $\delta^{18}O$ values when the moisture originates from the BoB than from the
733   Pacific Ocean, consistent with stronger convection during transport. The dominance of oceanic
734   moisture results in the lower vapor d-excess in eastern China (green arrow), whereas continental
735   recycling produces higher vapor d-excess in western and northwestern China.

736   (3) Variation in temperature drive the seasonal variations of vapor $\delta^{18}O$ in northern China,
737 whereas convective activity along trajectories produces low vapor $\delta^{18}O$ curing the monsoon
738 season and drive the seasonal variation in south China. Seasonal d-excess variation reflects
739 different conditions in the sources of vapor: in southeastern China it is mainly due to differences
740 in the RH over the adjacent ocean surface, while in northwestern China it is mainly due to the
741 vapor transported by the Westerlies during the pre-monsoon period and a great contribution of
742 continental recycling during the monsoon period.

743
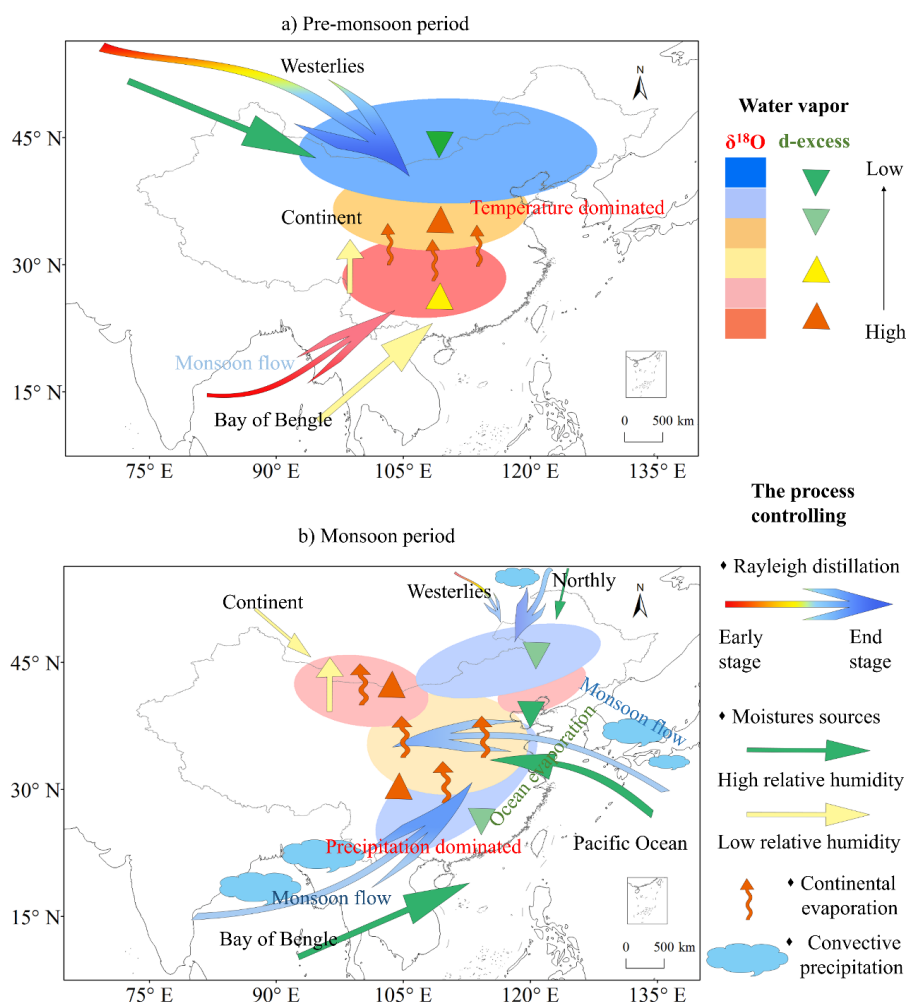
744 Fig.13 Schematic picture summarizing the different processes controlling the observed spatial
745 patterns and seasonality of vapor isotopes.

746

747   The Iso-GSM model captures the vapor $\delta^{18}O$ spatial pattern accurately during the pre-
748 monsoon period, likely due to the large latitudinal contrast in the humidity and temperature in
749 this season. However, the overall performance is weaker during the monsoon period. Modeling

Atmospheric
Chemistry
and Physics
Discussions

Open Access

EGU

750 results indicate that the observed temporal variations along the route across China are mainly
751 due to temporal-mean spatial variations, and marginally due to synoptic-scale variations.
752 Therefore, our observed snapshots provide the representative pictures of temporal-mean spatial
753 patterns.
754   Our study on the processes governing water vapor isotopic composition at the regional
755 scale provides an overview of the spatial distribution and seasonal variability of water isotopes
756 and their controlling factors, providing an improved framework for interpreting the
757 paleoclimate proxy records of the hydrological cycle in low and mid-latitudes. In particular, our
758 results suggest a strong interaction between local factors and circulation, emphasizing the need
759 to interpret proxy records in the context of the regional system. This also suggests the potential
760 for changes in circulation to confound interpretations of proxy data.

761 **Data availability**

762 The data acquired during the field campaigns and concurrent simulations from the isotope-
763 incorporated global spectral model (Iso-GSM) used has been submitted to the PANGEA
764 repository. The temporary link is https://issues.pangaea.de/browse/PDI-31288 and the final
765 DOI will be given as part of the revision process. This dataset can be provided by the
766 corresponding author upon request. Other data used can be downloaded from the corresponding
767 website which were listed in the text.

768 **Author contributions**

769 L.T. and D.W. designed the research; D.W., and X.J. conducted to the field observations; J.C.
770 and J. B. contribute to the data calibration; Z.W. and K.Y performed Iso-GCM simulations;
771 D.W., C.R., and L.T. performed analysis; All authors contributed to the discussion of the results
772 and the final article; D.W. drafted the manuscript with contributions from all co-authors; C.R.,
773 L.T. and J. B. checked and modified the manuscript.

774 **Competing interests**

775 The authors declare that they have no conflict of interest.

776 **Acknowledgments**

790 **References**

791 Araguás-Araguás, L., Froehlich, K., and Rozanski, K.: Stable isotope composition of precipitation over
792 southeast Asia, Journal of Geophysical Research: Atmospheres, 103, 28721-28742, 1998.

793 Bailey, A., Toohey, D., and Noone, D.: Characterizing moisture exchange between the Hawaiian
794 convective boundary layer and free troposphere using stable isotopes in water, Journal of Geophysical
795 Research: Atmospheres, 118, 8208-8221, 2013.

796 Benetti, M., Steen-Larsen, H. C., Reverdin, G., Sveinbjörnsdóttir, Á. E., Aloisi, G., Berkelhammer, M. B.,
797 Bourlès, B., Bourras, D., De Coetlogon, G., and Cosgrove, A.: Stable isotopes in the atmospheric marine
798 boundary layer water vapour over the Atlantic Ocean, 2012–2015, Scientific data, 4, 1-17, 2017.

799 Bonne, J.-L., Behrens, M., Meyer, H., Kipfstuhl, S., Rabe, B., Schönicke, L., Steen-Larsen, H. C., and Werner,
800 M.: Resolving the controls of water vapour isotopes in the Atlantic sector, Nature communications, 10,
801 1632, 2019.

802 Bony, S., Risi, C., and Vimeux, F.: Influence of convective processes on the isotopic composition ($\delta 18O$
803 and δD) of precipitation and water vapor in the tropics: 1. Radiative-convective equilibrium and Tropical
804 Ocean–Global Atmosphere–Coupled Ocean-Atmosphere Response Experiment (TOGA-COARE)
805 simulations, Journal of Geophysical Research: Atmospheres, 113, 2008.

806 Bowen, G. J., and Revenaugh, J.: Interpolating the isotopic composition of modern meteoric
807 precipitation, Water resources research, 39, 2003.

808 Bowen, G. J., Cai, Z., Fiorella, R. P., and Putman, A. L.: Isotopes in the Water Cycle: Regional-to Global-
809 Scale Patterns and Applications, Annual Review of Earth and Planetary Sciences, 47, 2019.

810 Brown, J., Simmonds, I., and Noone, D.: Modeling $\delta 18O$ in tropical precipitation and the surface ocean
811 for present-day climate, Journal of Geophysical Research Atmospheres, 111, -, 2006.

812 Cai, Z., and Tian, L.: Processes governing water vapor isotope composition in the Indo-Pacific region:
813 Convection and water vapor transport, Journal of Climate, 29, 8535-8546, 10.1175/JCLI-D-16-0297.1,
814 2016.

815 Cai, Z., Tian, L., and Bowen, G. J.: Spatial-seasonal patterns reveal large-scale atmospheric controls on
816 Asian Monsoon precipitation water isotope ratios, Earth and Planetary Science Letters, 503, 158-169,
817 2018.

818 Dansgaard, W.: Stable isotopes in precipitation, Tellus, 16, 436-468, 1964.

819 Domrös, M., and Peng, G.: The climate of China, Springer Science & Business Media, 2012.

820 Fiorella, R. P., Bares, R., Lin, J. C., Ehleringer, J. R., and Bowen, G. J.: Detection and variability of
821 combustion-derived vapor in an urban basin, Atmospheric Chemistry and Physics, 18, 8529-8547, 2018.

822 Fiorella, R. P., Bares, R., Lin, J. C., and Bowen, G. J.: Wintertime decoupling of urban valley and rural ridge
823 hydrological processes revealed through stable water isotopes, Atmospheric environment, 213, 337-
824 348, 2019.

825 Galewsky, J., and Hurley, J. V.: An advection-condensation model for subtropical water vapor isotopic
826 ratios, Journal of Geophysical Research Atmospheres, 115, 2010.

827 Galewsky, J., Rella, C., Sharp, Z., Samuels, K., and Ward, D.: Surface measurements of upper tropospheric

828   water vapor isotopic composition on the Chajnantor Plateau, Chile, Geophysical Research Letters, 38,
829   198-205, 2011.
830   Galewsky, J., Steen-Larsen, H. C., Field, R. D., Worden, J., Risi, C., and Schneider, M.: Stable isotopes in
831   atmospheric water vapor and applications to the hydrologic cycle, Reviews of Geophysics, 54, 2016.
832   Gao, J., MassonDelmotte, V., Risi, C., He, Y., and Yao, T.: What controls precipitation δ18O in the southern
833   Tibetan Plateau at seasonal and intra-seasonal scales? A case study at Lhasa and Nyalam, Tellus B, 65,
834   2013.
835   Gat, J. R., and Matsui, E.: Atmospheric water balance in the Amazon Basin: an isotopic
836   evapotranspiration model, Journal of Geophysical Research: Atmospheres, 96, 13179-13188, 1991.
837   Gat, J. R.: Oxygen and hydrogen isotopes in the hydrologic cycle, Annual Review of Earth and Planetary
838   Sciences, 24, 225-262, 1996.
839   Gorski, G., Strong, C., Good, S. P., Bares, R., Ehleringer, J. R., and Bowen, G. J.: Vapor hydrogen and
840   oxygen isotopes reflect water of combustion in the urban atmosphere, Proceedings of the National
841   Academy of Sciences, 112, 3247-3252, 2015.
842   Guo, X., Tian, L., Wen, R., Yu, W., and Qu, D.: Controls of precipitation δ 18 O on the northwestern
843   Tibetan Plateau: A case study at Ngari station, Atmospheric Research, 189, 141-151, 2017.
844   He, Y., Risi, C., Gao, J., Masson-Delmotte, V., Yao, T., Lai, C. T., Ding, Y., Worden, J., Frankenberg, C., and
845   Chepfer, H.: Impact of atmospheric convection on south Tibet summer precipitation isotopologue
846   composition using a combination of in situ measurements, satellite data, and atmospheric general
847   circulation modeling, Journal of Geophysical Research Atmospheres, 120, 3852-3871, 2015.
848   Hou, J., Huang, Y., Oswald, W. W., Foster, D. R., and Shuman, B.: Centennial-scale compound-specific
849   hydrogen isotope record of Pleistocene–Holocene climate transition from southern New England,
850   Geophysical Research Letters, 34, 2007.
851   JingfengLiu,   CundeXiao,   MinghuDing,   and   JiawenRen:
852   Variationsinstablehydrogenandoxygenisotopesinatmosphericwatervaporinthemarineboundarylayeracr
853   ossawidelatituderange, Journal of Environmental Sciences, 26, 2266-2276, 2014.
854   Johnson, K. R., and Ingram, B. L.: Spatial and temporal variability in the stable isotope systematics of
855   modern precipitation in China: implications for paleoclimate reconstructions, Earth and Planetary
856   Science Letters, 220, 365-377, 2004.
857   Jouzel, J., Alley, R., Cuffey, K., Dansgaard, W., Grootes, P., Hoffmann, G., Johnsen, S., Koster, R., Peel, D.,
858   and Shuman, C.: Validity of the temperature reconstruction from water isotopes in ice cores, Journal of
859   Geophysical Research: Oceans, 102, 26471-26487, 1997.
860   Kong, Y., and Pang, Z.: A positive altitude gradient of isotopes in the precipitation over the Tianshan
861   Mountains: Effects of moisture recycling and sub-cloud evaporation, Journal of Hydrology, 542, 222-230,
862   2016.
863   Kurita, N.: Origin of Arctic water vapor during the ice-growth season, Geophysical Research Letters, 38,
864   2011.
865   Li, Y., An, W., Pang, H., Wu, S. Y., Tang, Y., Zhang, W., and Hou, S.: Variations of Stable Isotopic
866   Composition in Atmospheric Water Vapor and their Controlling Factors—A 6-Year Continuous Sampling
867   Study in Nanjing, Eastern China, Journal of Geophysical Research Atmospheres, 125, 2020.
868   Liebmann, B., and Smith, C. A.: Description of a complete (interpolated) outgoing longwave radiation
869   dataset, Bulletin of the American Meteorological Society, 77, 1275-1277, 1996.
870   Liu, J., Song, X., Yuan, G., Sun, X., and Yang, L.: Stable isotopic compositions of precipitation in China,
871   Tellus B: Chemical and Physical Meteorology, 66, 22567, 2014.

872   Liu, Y., Cobb, K. M., Song, H., Li, Q., Li, C.-Y., Nakatsuka, T., An, Z., Zhou, W., Cai, Q., and Li, J.: Recent
873   enhancement of central Pacific El Niño variability relative to last eight centuries, Nature
874   communications, 8, 15386, 2017.
875   McKinney, C. R., McCrea, J. M., Epstein, S., Allen, H., and Urey, H. C.: Improvements in mass
876   spectrometers for the measurement of small differences in isotope abundance ratios, Review of
877   Scientific Instruments, 21, 724-730, 1950.
878   Mei'e, R., Renzhang, Y., and Haosheng, B.: An outline of China's physical geography, 1985.
879   Merlivat, L., and Jouzel, J.: Global climatic interpretation of the deuterium-oxygen 18 relationship for
880   precipitation, Journal of Geophysical Research: Oceans, 84, 5029-5033, 1979.
881   Noone, and David: Pairing Measurements of the Water Vapor Isotope Ratio with Humidity to Deduce
882   Atmospheric Moistening and Dehydration in the Tropical Midtroposphere, Journal of Climate, 25, 4476-
883   4494, 2012.
884   Noone, D.: The influence of midlatitude and tropical overturning circulation on the isotopic composition
885   of atmospheric water vapor and Antarctic precipitation, Journal of Geophysical Research: Atmospheres,
886   113, 2008.
887   Pfahl, S., and Sodemann, H.: What controls deuterium excess in global precipitation?, Climate of the
888   Past, 10, 771-781, 10.5194/cp-10-771-2014, 2014.
889   Putman, A. L., Fiorella, R. P., Bowen, G. J., and Cai, Z.: A global perspective on local meteoric water lines:
890   Meta-analytic insight into fundamental controls and practical constraints, Water Resources Research,
891   55, 6896-6910, 2019.
892   Risi, C., Bony, S., and Vimeux, F.: Influence of convective processes on the isotopic composition ($\delta18O$
893   and δD) of precipitation and water vapor in the tropics: 2. Physical interpretation of the amount effect,
894   Journal of Geophysical Research: Atmospheres, 113, -, 2008a.
895   Risi, C., Bony, S., Vimeux, F., Descroix, L., Ibrahim, B., Lebreton, E., Mamadou, I., and Sultan, B.: What
896   controls the isotopic composition of the African monsoon precipitation? Insights from event-based
897   precipitation collected during the 2006 AMMA field campaign, Geophysical Research Letters, 35, 851-
898   854, 2008b.
899   Risi, C., Noone, D., Worden, J., Frankenberg, C., Stiller, G., Kiefer, M., Funke, B., Walker, K., Bernath, P.,
900   Schneider, M., Wunch, D., Sherlock, V., Deutscher, N., Griffith, D., Wennberg, P. O., Strong, K., Smale, D.,
901   Mahieu, E., Barthlott, S., Hase, F., Garcia, O., Notholt, J., Warneke, T., Toon, G., Sayres, D., Bony, S., Lee,
902   J., Brown, D., Uemura, R., and Sturm, C.: Process-evaluation of tropospheric humidity simulated by
903   general circulation models using water vapor isotopologues: 1. Comparison between models and
904   observations, Journal of Geophysical Research-Atmospheres, 117, 10.1029/2011jd016621, 2012.
905   Risi, C., Landais, A., Winkler, R., and Vimeux, F.: Can we determine what controls the spatio-temporal
906   distribution of d-excess and 17 O-excess in precipitation using the LMDZ general circulation model?,
907   Climate of the Past, 9, 2173-2193, 2013a.
908   Risi, C., Noone, D., Frankenberg, C., and Worden, J.: Role of continental recycling in intraseasonal
909   variations of continental moisture as deduced from model simulations and water vapor isotopic
910   measurements, Water Resources Research, 49, 4136-4156, 2013b.
911   Roca, R., Chambon, P., Jobard, I., Kirstetter, P.-E., Gosset, M., and Bergès, J. C.: Comparing satellite and
912   surface rainfall products over West Africa at meteorologically relevant scales during the AMMA
913   campaign using error estimates, Journal of Applied Meteorology and Climatology, 49, 715-731, 2010.
914   Salati, E., Dall'Olio, A., Matsui, E., and Gat, J. R.: Recycling of water in the Amazon basin: an isotopic
915   study, Water resources research, 15, 1250-1258, 1979.

Atmospheric
Chemistry
and Physics
Discussions

916   Salmon, O. E., Welp, L. R., Baldwin, M. E., Hajny, K. D., Stirm, B. H., and Shepson, P. B.: Vertical profile
917   observations of water vapor deuterium excess in the lower troposphere, Atmospheric Chemistry and
918   Physics, 19, 11525-11543, 2019.
919   Samuels-Crow, K. E., Galewsky, J., Sharp, Z. D., and Dennis, K. J.: Deuterium excess in subtropical free
920   troposphere water vapor: Continuous measurements from the Chajnantor Plateau, northern Chile,
921   Geophysical Research Letters, 41, 8652-8659, 2015.
922   Shi, X., Risi, C., Pu, T., Lacour, J. l., Kong, Y., Wang, K., He, Y., and Xia, D.: Variability of isotope composition
923   of precipitation in the southeastern Tibetan Plateau from the synoptic to seasonal time scale, Journal
924   of Geophysical Research: Atmospheres, 125, e2019JD031751, 2020.
925   Steen-Larsen, H. C., Johnsen, S., Masson-Delmotte, V., Stenni, B., Risi, C., Sodemann, H., Balslev-Clausen,
926   D., Blunier, T., Dahl-Jensen, D., and Ellehøj, M. D.: Continuous monitoring of summer surface water
927   vapor isotopic composition above the Greenland Ice Sheet, Atmospheric Chemistry and Physics, 13,
928   4815-4828, 2013.
929   Steen-Larsen, H. C., Risi, C., Werner, M., Yoshimura, K., and Masson-Delmotte, V.: Evaluating the skills of
930   isotope-enabled General Circulation Models against in-situ atmospheric water vapor isotope
931   observations, Journal of Geophysical Research, 122, 246-263, 2017.
932   Tan, M.: Circulation effect: response of precipitation delta O-18 to the ENSO cycle in monsoon regions
933   of China, Climate Dynamics, 42, 1067-1077, 10.1007/s00382-013-1732-x, 2014.
934   Terzer-Wassmuth, S., Wassenaar, L. I., Welker, J. M., and Araguás-Araguás, L. J.: Improved high-
935   resolution global and regionalized isoscapes of δ 18O, δ 2H and d-excess in precipitation, Hydrological
936   Processes, 35, e14254, 2021.
937   Thompson, L. G.: Ice core evidence for climate change in the Tropics: implications for our future,
938   Quaternary Science Reviews, 19, 19-35, 10.1016/s0277-3791(99)00052-9, 2000.
939   Thurnherr, I., Kozachek, A., Graf, P., Weng, Y., Bolshiyanov, D., Landwehr, S., Pfahl, S., Schmale, J.,
940   Sodemann, H., and Steen-Larsen, H. C.: Meridional and vertical variations of the water vapour isotopic
941   composition in the marine boundary layer over the Atlantic and Southern Ocean, Atmospheric
942   Chemistry and Physics, 20, 5811-5835, 2020.
943   Tian, L., Yao, T., Schuster, P. F., White, J. W. C., Ichiyanagi, K., Pendall, E., Pu, J., and Yu, W.: Oxygen-18
944   concentrations in recent precipitation and ice cores on the Tibetan Plateau, Journal of Geophysical
945   Research Atmospheres, 108, -, 2003.
946   Tian, L., Yao, T., Li, Z., MacClune, K., Wu, G., Xu, B., Li, Y., Lu, A., and Shen, Y.: Recent rapid warming trend
947   revealed from the isotopic record in Muztagata ice core, eastern Pamirs, Journal of Geophysical
948   Research: Atmospheres, 111, 2006.
949   Tian, L., Yao, T., MacClune, K., White, J. W. C., Schilla, A., Vaughn, B., Vachon, R., and Ichiyanagi, K.: Stable
950   isotopic variations in west China: A consideration of moisture sources, Journal of Geophysical Research-
951   Atmospheres, 112, 10.1029/2006jd007718, 2007.
952   Tian, L., Yu, W., Schuster, P. F., Wen, R., Cai, Z., Wang, D., Shao, L., Cui, J., and Guo, X.: Control of seasonal
953   water vapor isotope variations at Lhasa, southern Tibetan Plateau, Journal of Hydrology, 580, 124237,
954   2020.
955   Van Breukelen, M., Vonhof, H., Hellstrom, J., Wester, W., and Kroon, D.: Fossil dripwater in stalagmites
956   reveals Holocene temperature and rainfall variation in Amazonia, Earth and Planetary Science Letters,
957   275, 54-60, 2008.
958   Vuille, M., and Werner, M.: Stable isotopes in precipitation recording South American summer monsoon
959   and ENSO variability: observations and model results, Climate Dynamics, 25, 401-413, 2005.

960 Wang, B., and Xu, X.: Northern Hemisphere summer monsoon singularities and climatological
961 intraseasonal oscillation, Journal of Climate, 10, 1071-1085, 1997.

962 Wang, B.: Rainy season of the Asian–Pacific summer monsoon, Journal of Climate, 15, 386-398, 2002.

963 Wang, D., and Wang, K.: Isotopes in precipitation in China (1986–1999), Science in China Series E:
964 Technological Sciences, 44, 48-51, 2001.

965 West, J. B., Bowen, G. J., Dawson, T. E., and Tu, K. P.: Isoscapes: understanding movement, pattern, and
966 process on Earth through isotope mapping, Springer, 2009.

967 Winnick, M. J., Chamberlain, C. P., Caves, J. K., and Welker, J. M.: Quantifying the isotopic 'continental
968 effect', Earth and Planetary Science Letters, 406, 123-133, 2014.

969 Worden, J., Noone, D., Bowman, K., and Tropospheric Emission, S.: Importance of rain evaporation and
970 continental convection in the tropical water cycle, Nature, 445, 528-532, 10.1038/nature05508, 2007.

971 Wright, H. E.: Global climates since the last glacial maximum, U of Minnesota Press, 1993.

972 Yang, H., Johnson, K. R., Griffiths, M. L., and Yoshimura, K.: Interannual controls on oxygen isotope
973 variability in Asian monsoon precipitation and implications for paleoclimate reconstructions, Journal of
974 Geophysical Research Atmospheres, 121, 8410–8428, 2016.

975 Yao, T., Ding, L., Pu, J., Liu, J., and Yang, Z.: Characteristic of δ18O in snow and its relation with moisture
976 sources in Tanggula Mountains, Tibetan Plateau, Chinese Science Bulletin, 36, 1570-1573, 1991.

977 Yoshimura, K., and Kanamitsu, M.: Specification of External Forcing for Regional Model Integrations,
978 Mon.wea.rev, 137, 1409-1421, 2009.

979 Zhao, L., Xiao, H., Zhou, M., Cheng, G., Wang, L., Yin, L., and Ren, J.: Factors controlling spatial and
980 seasonal distributions of precipitation δ18O in China, Hydrological Processes, 26, 143-152, 2012.

981